

Review Article

Generalised receiver functions and seismic interferometry

Erica Galetti ^{a,*}, Andrew Curtis ^{a,b,c}^a School of GeoSciences, University of Edinburgh, Grant Institute, King's Buildings, Edinburgh EH9 3JW, United Kingdom^b School of Geography, Environment and Earth Sciences, Victoria University of Wellington, PO Box 600, Wellington, New Zealand^c GNS Science, 1 Fairway Drive, Avalon 5010, PO Box 30–368, Lower Hutt 5040, New Zealand

ARTICLE INFO

Article history:

Received 23 February 2011

Received in revised form 25 October 2011

Accepted 2 December 2011

Available online 13 December 2011

Keywords:

Seismic

Interferometry

Receiver functions

Seismology

Imaging

Subsurface

ABSTRACT

Classical seismological receiver functions are correlational or deconvolutional combinations of vertical and horizontal component seismometer recordings of earthquake waves that focus information on near-receiver subsurface Earth structure and properties. We show that seismic interferometry can be thought of as a generalisation of receiver functions analysis to cases where recordings at pairs of receivers are considered simultaneously, and where either the same or different component recordings are combined. Further, seismic interferometry uses any of deconvolution, convolution and cross-correlation, and energy from either impulsive or random noise sources. We show both how receiver functions can logically be extended to a new, convolutional form, and that the now little-used correlational form of receiver functions contains more intuitive information than previously realised.

Seismic interferometry has provided other extraordinary extensions to seismologists' arsenal. Passive noise recordings can be converted into seismograms from virtual (imagined) earthquakes that in turn can be used to image the real Earth. Active sources (e.g., earthquakes or man-made sources) can be redatumed into new, virtual sources elsewhere, or can be converted into virtual sensors (seismometers) that record seismograms from other real earthquakes, man-made sources or noise sources that occur either in the future or in the past. And the ability to construct virtual sources and sensors at desired times and locations (rather than having to wait for earthquake sources that occur at uncontrollable locations) promises more repeatable monitoring of changes in Earth subsurface properties over time. Indeed, so-called coda wave interferometry offers unprecedented accuracy in detecting such changes. Finally, existing theoretical extensions to other regimes such as electromagnetic, electrokinetic and diffusive energy propagation may lead to future revolutions in other domains of science.

© 2012 Elsevier B.V. All rights reserved.

Contents

1. Introduction	2
2. Classical receiver functions	2
3. Non-classical receiver functions	3
4. Background to the theory of seismic interferometry	4
5. Theory of inter-receiver interferometry	7
5.1. Interferometry and Time-Reversed Acoustics	7
5.2. Interferometry and Reciprocity	8
5.3. Stationary-Phase Approach	9
6. Applications of inter-receiver interferometry	13
7. Inter-source interferometry	18
8. Source-receiver interferometry	19
9. Time-dependent monitoring and green's functions from late seismic codas	21
10. Discussion	23
Acknowledgements	24
References	24

* Corresponding author. Tel.: +44 131 650 5919; fax: +44 131 668 3184.

E-mail address: E.Galetti@sms.ed.ac.uk (E. Galetti).

1. Introduction

Seismic interferometry loosely refers to a range of methods within which seismograms that were not physically recorded, are estimated by cross-correlation, convolution or deconvolution and summation of other recorded wavefields (Campillo and Paul, 2003; Claerbout, 1968; Duvall et al., 1993; Lobkis and Weaver, 2001; Rickett and Claerbout, 1999; Shapiro and Campillo, 2004; Snieder, 2004; van Manen et al., 2005; 2006; 2007; Wapenaar, 2004; Wapenaar and Fokkema, 2006; Wapenaar et al., 2010a; 2010c; Weaver and Lobkis, 2001). This apparently benign ability has had profound implications for seismology.

For example, it is now possible to create estimates of inter-receiver surface waves (surface waves that would have been recorded at one receiver location if there had been a source at the location of the other) using passive or ambient seismic noise – the part of seismic recordings that until recently were filtered out of data to be analysed. This is of great interest to seismologists since passive noise sources can thus be used to create seismic velocity maps or profiles in global, regional or industrial scale seismology using human-designed, inter-receiver networks of wave propagation or ray paths (Gerstoft et al., 2006; Halliday and Curtis, 2008; Moschetti et al., 2007; Sabra et al., 2005; Shapiro and Campillo, 2004; Shapiro et al., 2005; Snieder, 2004; Snieder et al., 2006; Yang et al., 2007). It is also possible to obtain inter-receiver body wave estimates from ambient noise fields, but this is far more difficult due to the low body wave energy in naturally occurring ambient noise (Draganov et al., 2006; 2007; 2009; Forghani and Snieder, 2010; Miyazawa et al., 2008; Ruigrok et al., 2010; Tonegawa and Nishida, 2010; Tonegawa et al., 2009; Zhan et al., 2010).

Actively induced or impulsive source signals can also be cross-correlated to synthesise new, inter-receiver wavefield estimates (Bakulin and Calvert, 2006; King et al., 2011; Lu et al., 2008; Slob et al., 2007). For example, Curtis et al. (2006), Dong et al. (2006), Halliday et al. (2007, 2010a) propose that similar inter-receiver surface wave estimates to those above can be used as part of a ground-roll (surface-wave) removal method in exploration seismology. Halliday et al. (2008) demonstrate that it is possible to recover both fundamental and higher-mode inter-receiver surface waves, with specific geometrical dependencies predicted by Halliday and Curtis (2008). Similar techniques can produce novel schemas for computational full-wavefield modelling (van Manen et al., 2005, 2006, 2007), and King et al. (2011) show that active-source interferometry offers new approaches to subsurface velocity analysis. More recently, *interferometry by deconvolution* (Vasconcelos and Snieder, 2008a, 2008b; Wapenaar and van der Neut, 2010; Wapenaar et al., 2011) has been proposed as an alternative technique to cross-correlational interferometry in cases where the recorded wavefields present a strong source signature, or where the distribution of sources is not uniform in space.

By using two different forms of interferometry, Hong and Menke (2006) and Curtis et al. (2009) show that it is also possible to estimate inter-source seismograms (as though one of a pair of sources had been a seismometer that recorded the other source) using earthquake sources as subsurface seismometers. The latter method was applied by Tonegawa and Nishida (2010) to find body wave travel times between earthquakes in the slab subducting beneath Japan.

As can be seen from the references cited above, while this field has its origins in a handful of papers from before 2000, it has expanded dramatically in terms of both theoretical development and practical use since only 2003. In that year both the first solid-Earth application was demonstrated (Campillo and Paul, 2003), and the first comprehensive 3-dimensional mathematical theory was published (Wapenaar, 2003). The field may therefore still be in its infancy. Nevertheless, advances are already such that it is timely for Earth scientists in a variety of fields to become familiar with these techniques, and to investigate what they offer in these various fields of application.

This paper begins by showing how seismic interferometry can be thought of as a generalisation of conventional seismological (deconvolutional and cross-correlational) receiver function analysis. It then gives a more detailed review of interferometric theory and applications. Finally, it explores implications of seismic interferometry for future tectonophysical studies.

2. Classical receiver functions

In order to understand the near-surface (e.g., crustal and upper-mantle) structure beneath a seismometer, it is common to calculate so-called receiver functions (Phinney, 1964; Vinnik, 1977). If waves emanating from some distant source impinge on a subsurface interface between layers of different elastic properties (the Moho for example), the energy both refracts and converts from P to S energy or vice versa as it crosses the interface. This energy may then be recorded at a seismometer. If the energy source is far from the seismometer, the path of propagation at and below the seismometer is usually reasonably close to vertical due to refraction in near-surface, low-velocity layers. In that case the P energy appears dominantly on the vertical-component recording, shear energy on the horizontal components (Fig. 1(a)).

A receiver function is a quantity derived from the P (or vertical-component $V(t)$) and S (horizontal-component $H(t)$) seismograms designed such that it focuses information on the propagation path between the interface and the seismometer, diminishing sensitivity to Earth properties along the rest of the path of propagation. Usually this involves transforming the vertical and horizontal components into the frequency domain and dividing one by the other for each frequency – an operation known as deconvolution:

$$R(\mathbf{x}, \omega) = \frac{H(\mathbf{x}, \omega)}{V(\mathbf{x}, \omega)}, \quad (1)$$

where ω is angular frequency and \mathbf{x} is the location of the recording. Intuitively, parts of the data that are common to both the vertical and horizontal recordings will cancel out between numerator and denominator. Parts that are approximately common correspond to the propagation path before the interface was intercepted by the wavefield (lower left in Fig. 1(a)). Hence, what remains after this division is a quantity R that is dominantly sensitive to the structure at and above the reflector. R is known as a receiver function, and would subsequently be used to infer the distribution of properties of the near-surface approximately beneath the receiver location (Gurrola et al., 1994; Heit et al., 2008; Langston, 1979; Ryberg and Weber, 2000; van Manen et al., 2003; Vinnik, 1977).

In reality the division is stabilised to avoid problems with division by zero for any frequency. For example, the water level method of Langston (1979) simply sets the magnitude of the denominator equal to some fixed, small number e if it is ever less than e . In addition, many alternative methods of receiver function retrieval exist such as plain summation without deconvolution (Kumar et al., 2010), and the deconvolution technique may simply be employed to enhance signal-to-noise ratios. Nevertheless, Eq. (1) represents the essential elements of a receiver function and provides a natural link to the theory of seismic interferometry.

To this end, notice that a receiver function can be thought of in a slightly different way by multiplying numerator and denominator by the complex conjugate of the denominator:

$$\frac{H(\omega)}{V(\omega)} = \frac{H(\omega)V^*(\omega)}{V(\omega)V^*(\omega)} = \frac{1}{|V(\omega)|^2} H(\omega)V^*(\omega), \quad (2)$$

where we have omitted the \mathbf{x} -dependence for the moment. The final term includes the cross-correlation of H and V (since cross-correlation of two time-series is defined in the frequency domain as the

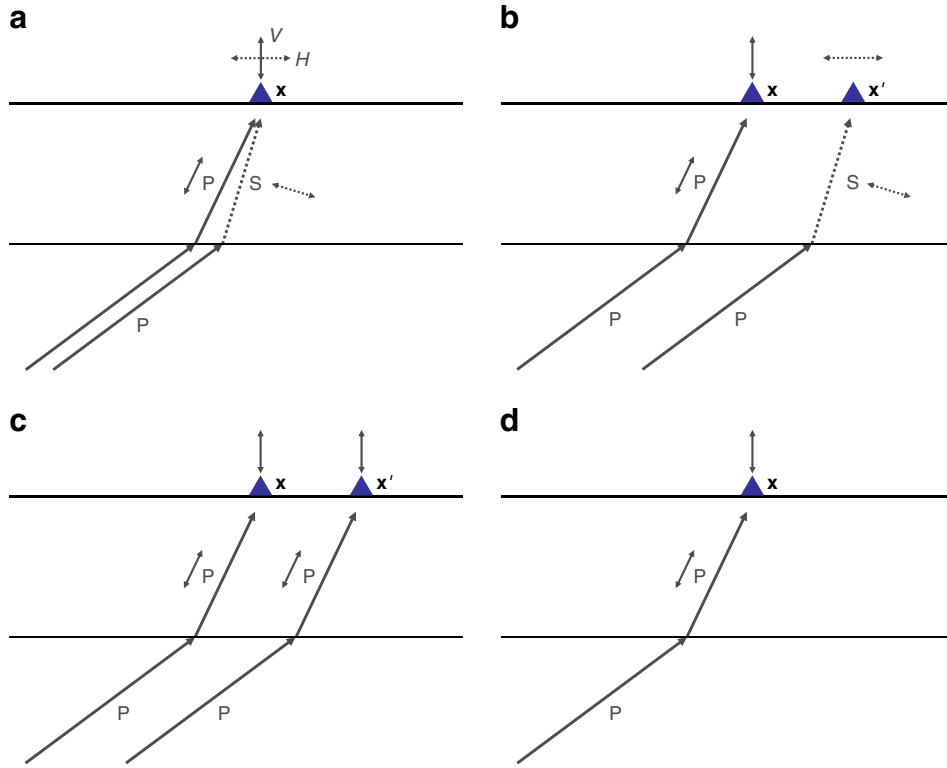


Fig. 1. Non-classical receiver function analysis. (a) A vertical and a horizontal sensor are placed side by side and record P and S arrivals. (b) The two sensors are moved apart. (c) The horizontal sensor is replaced by a vertical sensor. (d) The two vertical sensors are moved back side by side.

multiplication of one with the conjugate of the other for each frequency), and thus we see that receiver function R is nothing more than a cross-correlation of H and V , weighted by a set of real numbers ($1/|V(\omega)|^2$). Indeed, the cross-correlation includes all phase information in the receiver function, and it is interesting to note that some earlier work on receiver functions used the cross-correlation rather than the deconvolution of H and V (Kind and Vinnik, 1988). From hereon we will therefore consider a classical receiver function R_C to be simply a (perhaps weighted) cross-correlation of a vertical and a horizontal component record:

$$R_C(\mathbf{x}, \omega) \cong H(\mathbf{x}, \omega)V^*(\mathbf{x}, \omega). \quad (3)$$

3. Non-classical receiver functions

We now introduce a *non*-classical extension to receiver functions analysis. Within every multi-component seismometer there are multiple sensors, each measuring the displacement (or time-derivatives thereof) in different directions. Instead of encasing them all within one seismometer, let us imagine them as each having separate casings. If we put a vertical-component sensor beside a horizontal-component sensor and make a recording of the situation in Fig. 1(a) we will obtain essentially identical records to those discussed above. However, we are then free to move these two sensors apart from each other as in Fig. 1(b).

We can still calculate the cross-correlation of the two recordings

$$R^{HV}(\mathbf{x}, \mathbf{x}', \omega) = H(\mathbf{x}, \omega)V^*(\mathbf{x}', \omega), \quad (4)$$

but in this case the non-classical receiver function R^{HV} depends on both locations \mathbf{x} and \mathbf{x}' (van Manen, 2006). It is not obvious that it will be any easier to interpret R^{HV} than it would the original recordings of V and H : the portion of the path up to the interface is now

not necessarily even approximately the same, and hence it is not obvious that R^{HV} contains information that is focussed on the portion of the subsurface that is close to the two receivers. Nevertheless we can still choose to calculate R^{HV} and below we will show that in fact R^{HV} can be converted into something that is as easy to interpret as a standard seismogram.

Given that R^{HV} is calculated between two separate seismometers, it is also possible to replace the right-hand horizontal component sensor with another vertical component sensor as in Fig. 1(c), and calculate the cross-correlation,

$$R^{VV}(\mathbf{x}, \mathbf{x}', \omega) = V(\mathbf{x}, \omega)V^*(\mathbf{x}', \omega) \quad (5)$$

and indeed it is possible to move the two vertical-component sensors side by side as in Fig. 1(d) and calculate

$$R^{VV}(\mathbf{x}, \omega) = V(\mathbf{x}, \omega)V^*(\mathbf{x}, \omega). \quad (6)$$

The right side of Eq. (6) is the autocorrelation of the vertical record with itself.

To get to this point it has been necessary to take steps that are not usually taken in receiver functions analysis, yet the result is remarkably similar to the classical formula in Eq. (3). However, in retrospect we now recognise Eq. (6) as the first published example of seismic interferometry: if $V(\mathbf{x}, \omega)$ is a recording of the arriving P wave and all of its subsequent reverberations (multiples) within the medium (the Earth) as shown in Fig. 2(a), then the recording is an approximation to the so-called *transmission response* of the medium – the measurement one would obtain on one side of the medium of waves transmitted from a temporally impulsive source on the far side of the medium. Claerbout (1968) proved that the autocorrelation of the acoustic transmission response in Fig. 2(a) is equal to the so-called *reflection response* depicted in Fig. 2(b) – the seismogram that one would have recorded if the impulsive source was instead placed

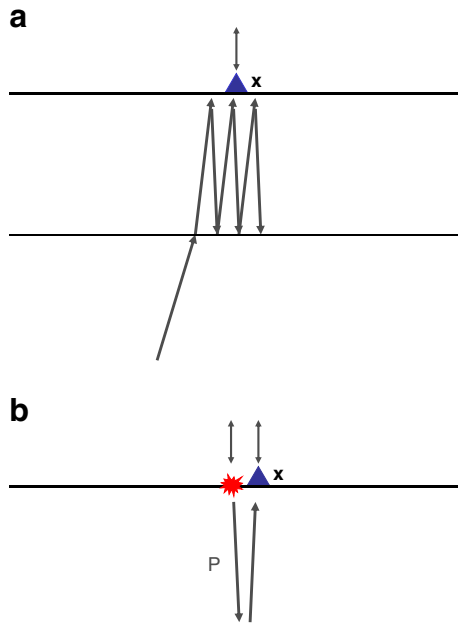


Fig. 2. From transmission to reflection response: (a) the transmission response is given by the arriving P wave and all of its reverberations in the subsurface. (b) The reflection response is obtained from the autocorrelation of the transmission response.

on the near side of the medium. That is, by autocorrelation we obtain a real seismogram from a source that never actually existed; we now call such sources *virtual* (imagined) sources.

The far-reaching importance of this result was embodied within a conjecture made by Claerbout, quoted by Cole (1995) and Rickett and Claerbout (1999): that in the geometrical case depicted in Fig. 1(c) it would be possible that the cross-correlation of the recordings made at the two receivers in Eq. (5) would also result in a seismogram from a virtual source at the surface. This result was subsequently demonstrated by Rickett and Claerbout (1999) for the sun, and by Campillo and Paul (2003) for the Earth, and was eventually proved to be true mathematically by Wapenaar (2003, 2004). Wapenaar showed that the conjecture is true provided that the transmission response is recorded from sources that (in a sense made strict below) surround the portion of the medium that contains the two receivers as in Fig. 3(a). Intuitively, by recording at two points the energy from this set of impulsive sources that surround this portion of the medium, and by cross-correlating and summing over all of those recordings, we obtain the real seismogram from a virtual source, and Wapenaar proved that the virtual source would be at the location of one of the two receivers as in Fig. 3(b).

We think of this simple data processing operation of cross-correlation and summation, now called seismic interferometry, as having turned a real receiver into a virtual source, from which we obtain a real seismogram. What is more, Wapenaar (2003, 2004) proved that this would also hold approximately true if instead of being impulsive the sources were uncorrelated ambient noise sources that possibly fire contemporaneously, and hence which are already summed within the recordings. In principle then, by recording at two points the background noise in the Earth from diverse uncorrelated sources throughout and around the Earth, then cross-correlating these two recordings, a seismogram is obtained that approximates what one would have recorded if a real source had existed at the location of one of the seismometers. Thus we obtain real, earthquake-like seismograms without the need for an earthquake to occur.

The implications for seismology have been profound. Most of the Earth has virtually no large local earthquakes (Fig. 4). Such areas can not easily be imaged in detail using conventional seismological

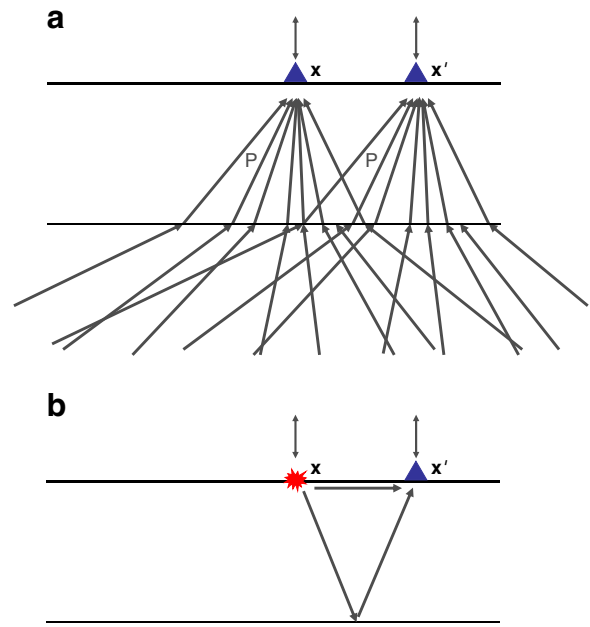


Fig. 3. Principle of seismic interferometry. (a) Two receivers record P-wave arrivals from sources within the medium. (b) Cross-correlation of these recordings turns one of these receivers into a virtual source, whose signal is recorded at the other receiver.

methods other than by classical receiver functions analysis as in Eqs. (1) and (3), and even then only approximately vertically beneath each individual receiver. Local tomography or imaging between receiver locations is difficult because while we can install local seismometer arrays, such areas have no local sources so that all recorded seismograms have very long source-to-receiver ray paths. Discriminating only the local component of such recordings is difficult. On the other hand, by using seismic interferometry, if long recordings of background noise are taken at any set of local receivers, and for every pair of receivers these recordings are then cross-correlated, we convert each receiver in turn into a virtual source and obtain real seismogram recordings of that source at all of the other receivers. Thus we obtain a local array of source-to-receiver records that can be analysed for detailed structure both beneath and between receivers in the array, and in principle we can do this anywhere that we can put receivers on the surface of the dominantly aseismic Earth.

The remainder of this article explores the historical background of seismic interferometry, and presents the mathematical results that form a necessary foundation of knowledge in order to understand and apply this theory robustly. It then explores the consequences of this theory which, in the space of only eight years since the first mathematical proof, has revolutionised the imaging of much of the Earth's crust and upper mantle, and has led to the creation of methods to monitor temporal changes in the Earth that are so exceptionally accurate as to be unimaginable only a decade ago. We have already shown that seismic interferometry can be thought of as a generalisation of receiver functions analysis, and we will show later that interferometry expands the field of receiver functions analysis from only correlation and deconvolution to a third form, involving convolution of records. The result is a theory that has revolutionised Earth imaging while still in its infancy, and which will certainly have many significant consequences still unimagined today.

4. Background to the theory of seismic interferometry

The first derivation of seismic interferometric theory was published for 1D media by Claerbout (1968), and extended using modal

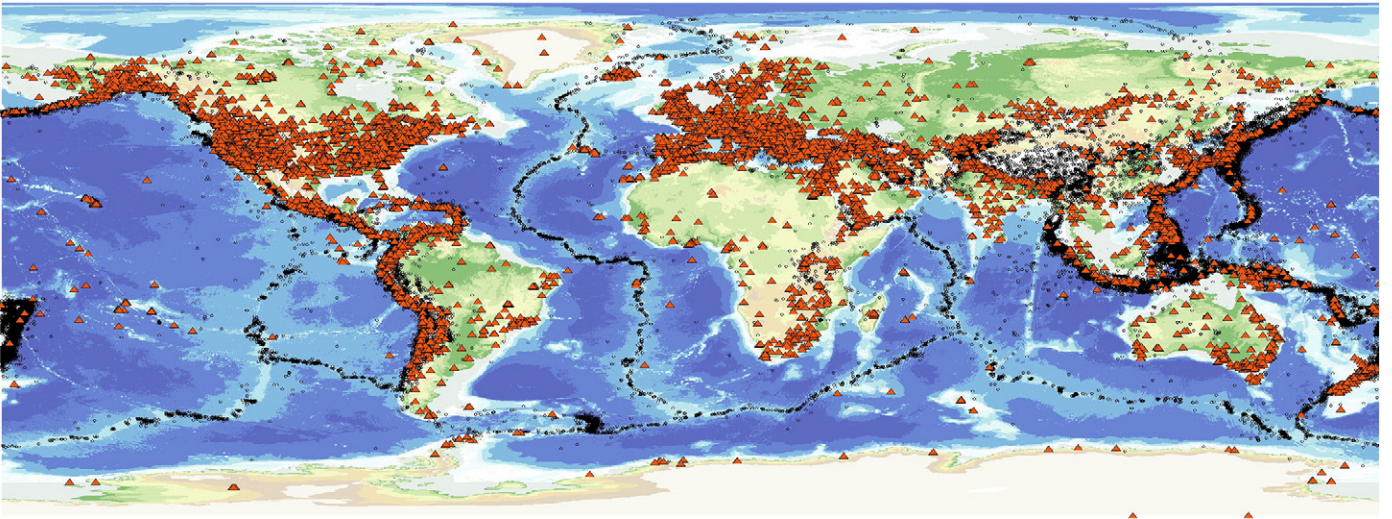


Fig. 4. Global distribution of National Earthquake Information Center (NEIC) seismometers (triangles) and earthquakes of magnitude > 5 since 1973 (circles). Map courtesy of Brian Baptie (British Geological Survey).

theory by Weaver and Lobkis (2001) and Lobkis and Weaver (2001). It was eventually proved for fully 3D acoustic media (Wapenaar, 2003; van Manen et al., 2005, 2006; Wapenaar et al., 2010a, 2010c), elastic media (Wapenaar, 2004; Snieder et al., 2006; van Manen et al., 2006; Wapenaar and Fokkema, 2006) and electromagnetic media (Slob et al., 2007; Slob and Wapenaar, 2007), and a unified approach allows application to other wave phenomena such as seismoelectric wave propagation and diffusive wavefields (Wapenaar et al., 2006; Snieder et al., 2007; Vasconcelos, 2008). Although they can be quite complex, we explore some of these different derivations here as they shed light on the generality of interferometric theory, provide intuition about *why* interferometry works, and highlight the approximations made when interferometry is applied in practice. The latter is particularly important for robust interpretation of results of interferometric studies.

Let us now consider the 1D configuration shown in Fig. 5(a): a homogeneous, lossless acoustic layer of thickness Δz and propagation velocity c , is sandwiched between a stress-free surface (like the Earth's surface) and a homogeneous lossless half-space. The upwards-travelling transmission coefficient across the subsurface interface is τ . A vertically upward-propagating wave is emitted by an impulsive unit source in the lower half-space, and arrivals are recorded at a point on the free surface. These arrivals are shown in Fig. 5(b): the first arrival occurs at time t_0 and has amplitude $a_0 = \tau$; the second arrival, resulting from the wave being reflected downwards by the free surface (with reflection coefficient -1) and then upwards by the interface (with reflection coefficient r), occurs at time $t_0 + \Delta t$ (with $\Delta t = 2\Delta z/c$) and has amplitude $a_1 = -r\tau$; subsequent arrivals occur at regular time intervals Δt , and have amplitudes $a_2 = r^2\tau$, $a_3 = -r^3\tau$, etc. If we denote the global transmission response by $T(t)$ and its time-reverse by $T(-t)$, then the autocorrelation of the global transmission response (i.e. the convolution of the signal with its time-reverse) yields the global reflection response:

$$T(t) * T(-t) = \delta(t) - R(t) - R(-t), \quad (7)$$

where the star (*) denotes convolution, $\delta(t)$ is the impulse obtained from autocorrelation for zero lag time, and $R(t)$ and $R(-t)$ are the so-called causal and acausal parts of the autocorrelation, respectively (Wapenaar, 2003; Wapenaar et al., 2010a). An intuitive representation of all terms in Eq. (7) is given in Fig. 5(c).

By rearranging the terms in Eq. (7), we obtain the so-called *Kunetz equation* (Claerbout, 1976):

$$R(t) + R(-t) = \delta(t) - T(t) * T(-t). \quad (8)$$

According to Eq. (8), the Earth's reflection response (from a plane wave source at the surface, a source which did not exist) can be constructed by taking either the positive- or negative-time part of the autocorrelation of its transmission response.

In the case of transient, non-impulsive sources (e.g., ambient noise), Eq. (8) can be modified as follows (Claerbout, 1968):

$$\{R(t) + R(-t)\} * S_N(t) = S_N(t) - \langle u(t) * u(-t) \rangle, \quad (9)$$

where $N(t)$ is the noise signal emitted by the source in the lower half-space, $u(t) = T(t) * N(t)$ is the recorded wavefield at the surface and $S_N(t) = N(t) * N(-t)$ is the autocorrelation of the noise source time function. According to Eq. (9), an approximation to the Earth's reflection response can be obtained from the autocorrelation of passive noise transmission records. The theory can be proved to hold for arbitrarily layered media (Claerbout, 1968).

Claerbout conjectured that the method could be extended to 2D and 3D varying media and wavefields, but it was not until 1993 that this was shown to be applicable in reality: Duvall et al. (1993) and Rickett and Claerbout (1999) applied cross-correlation to records of solar surface noise to obtain the first helioseismological pseudo-impulsive shot records.

Mathematical proofs of 3D seismic interferometry based on representation theorems were derived subsequently by Wapenaar (2003, 2004), van Manen et al. (2005, 2006), Wapenaar and Fokkema (2006), Wapenaar et al. (2006), Slob et al. (2007), Snieder et al. (2007), Vasconcelos (2008), and Wapenaar and van der Neut (2010), and based on a stationary-phase approach by Snieder (2004). The theory has been independently demonstrated through time-reversal laboratory experiments by Lobkis and Weaver (2001), Weaver and Lobkis (2001), Derode et al. (2003a, 2003b) and Larose et al. (2005). All of these derivations have one element in common: by applying the above-mentioned techniques to the recordings obtained at a pair of receivers, a new set of data is obtained that approximates or equals that which would be recorded at one of the two receivers if the other one was instead at the location of an active

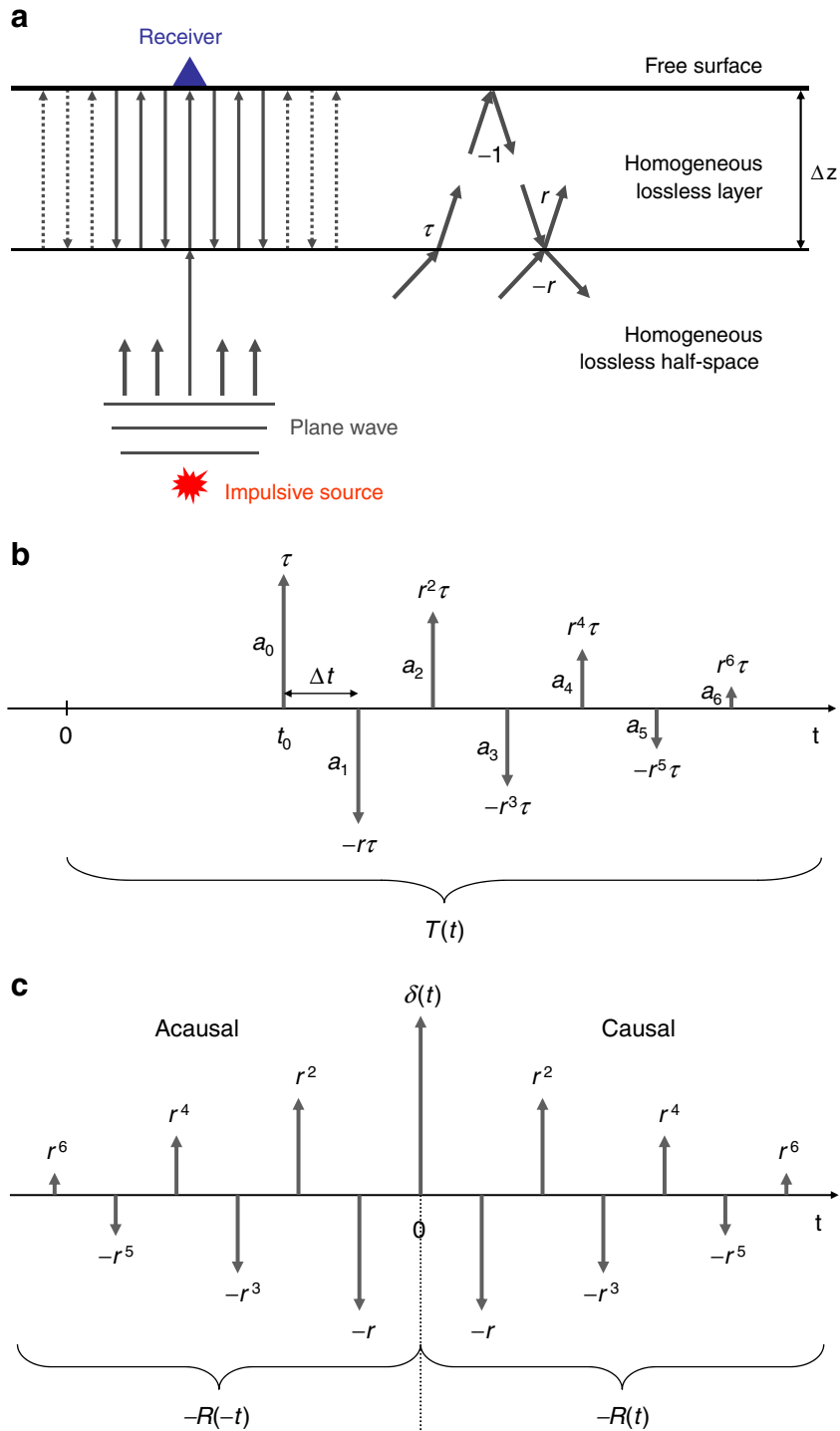


Fig. 5. From transmission to reflection response in 1D as conceived by Claerbout (1968). (a) Simple layered medium consisting of a homogeneous, lossless layer sandwiched between a lossless half-space and a free-surface. The transmission coefficient at the subsurface interface is τ , the reflection coefficient is r ; the reflection coefficient at the free surface is -1 . (b) Transmission response $T(t)$ as observed at a point on the free surface. (c) Autocorrelation of the transmission response $T(t) * T(-t)$ yields, apart from a negative sign, the reflection response $R(t)$ (causal part of the autocorrelation) and the time-reversed reflection response $R(-t)$ (acausal part of the autocorrelation). Redrawn after Wapenaar et al. (2010a).

source. This form of seismic interferometry is called *inter-receiver interferometry*, and it allows one of the receivers to be turned into a ‘virtual’ (imagined) source. However, inter-receiver interferometry is not the only type of interferometry as two additional forms have recently been developed: *inter-source interferometry* (Hong and Menke, 2006; Curtis et al., 2009), which allows a real source to be turned into a virtual receiver, and *source-receiver interferometry* (Curtis and Halliday, 2010a), which allows a (perhaps unrecorded) recording of energy

travelling between a source and a receiver to be constructed by making use of both virtual sources and virtual receivers.

The following sections of this article provide details of each of these three forms of interferometry, together with a number of successful examples of their application. Finally, the method of *coda-wave interferometry* (Snieder et al., 2002; Snieder, 2006) and its application to time-dependent monitoring are presented and discussed.

5. Theory of inter-receiver interferometry

5.1. Interferometry and Time-Reversed Acoustics

There is a precise link between Green's function retrieval in seismic interferometry and wavefields in time-reversed acoustics which provides an intuitive approach to understand interferometric theory. It was clearly illustrated by Derode et al. (2003a, 2003b) who, starting from the principle of invariance of the wave equation under time-reversal, derive Green's function representations using physical arguments.

Consider a lossless, arbitrarily inhomogeneous, acoustic medium bounded by surface S embedded within a homogeneous surrounding medium (Fig. 6). Suppose a source, located at position \mathbf{x}_A within the

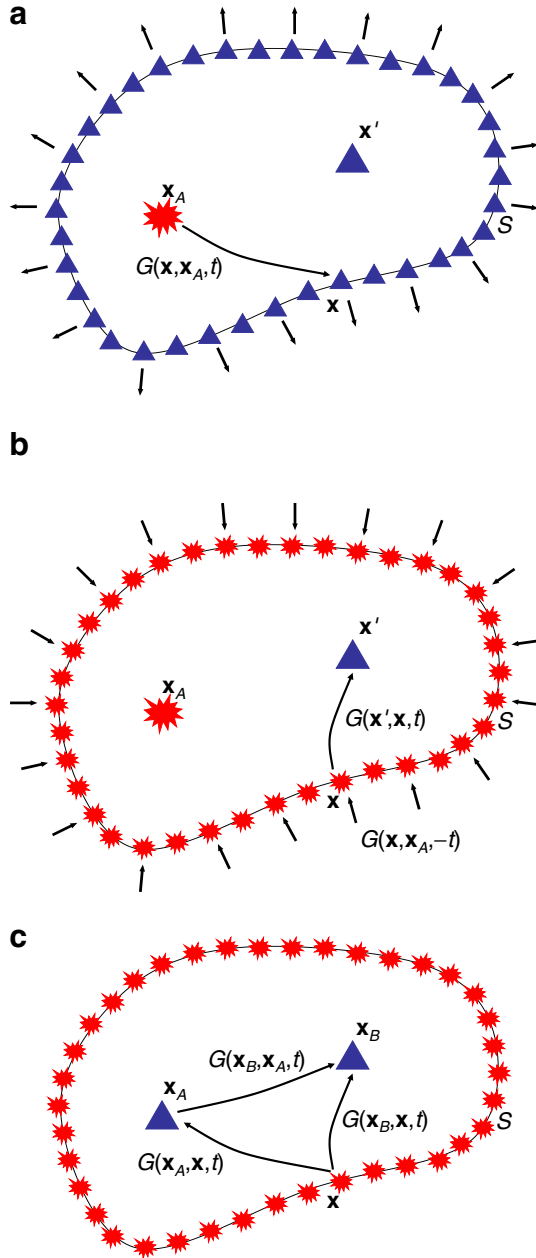


Fig. 6. Green's function retrieval from a time-reversed acoustics experiment. (a) The response at a receiver at \mathbf{x} on boundary S for a source at \mathbf{x}_A is given by $G(\mathbf{x}, \mathbf{x}_A, t)$. (b) The time-reversed signal $G(\mathbf{x}, \mathbf{x}_A, -t)$ is emitted back into the medium from sources on boundary S . (c) The Green's function between \mathbf{x}_A and \mathbf{x}_B can be obtained by cross-correlating the wavefield recorded at these two positions and integrating over the whole boundary. Redrawn after Wapenaar et al. (2010b).

inhomogeneous medium, fires an impulse at time $t=0$, and the response is recorded by receivers located at positions \mathbf{x} all around a boundary S (Fig. 6(a)). In the time domain, the response to the impulsive source at \mathbf{x}_A , recorded at each \mathbf{x} on S , is denoted by $G(\mathbf{x}, \mathbf{x}_A, t)$, and the time-reverse of this signal is denoted by $G(\mathbf{x}, \mathbf{x}_A, -t)$. If the time-reversed signals are simultaneously fed back into the medium by transducer sources at all positions \mathbf{x} on the boundary (Fig. 6(b)), in the absence of attenuation the wavefield should exactly reverse, arriving at any arbitrary position $\mathbf{x}' \neq \mathbf{x}$ (at $t < 0$) before refocusing at the original source location \mathbf{x}_A at time $t=0$ (just as the concentric waves originating from a stone dropped into a pond would travel inwards to refocus on the stone if we played the recording of the event backwards in time).

The wavefield recorded at point \mathbf{x}' inside boundary S , due to sources \mathbf{x} on boundary S , can be obtained by applying the superposition principle:

$$u(\mathbf{x}', t) \propto \int_S G(\mathbf{x}', \mathbf{x}, t) * G(\mathbf{x}, \mathbf{x}_A, -t) dS. \quad (10)$$

Here, the symbol \propto denotes proportionality, while the star (*) denotes convolution between the boundary source term $G(\mathbf{x}, \mathbf{x}_A, -t)$ (the time-reverse of the original boundary recordings) and the propagation term $G(\mathbf{x}', \mathbf{x}, t)$ which defines how the wave propagates from boundary location \mathbf{x} to any interior location \mathbf{x}' . The integral over S ensures that the contributions from all sources on the boundary are considered simultaneously.

However, as energy is not taken out of the system at $t=0$, the wavefield does not stop after refocusing at \mathbf{x}_A , but propagates outwards again, arriving at position \mathbf{x}' again at $t > 0$. This wavefield must be identical to the original wavefield propagating out from the source at \mathbf{x}_A (since no energy has been removed or altered in the time-reversed experiment); it must also be the time-reverse of the wavefield observed at \mathbf{x}' as the waves were converging towards \mathbf{x}_A . Hence, the wavefield $u(\mathbf{x}', t)$ that would be recorded at \mathbf{x}' consists of negative-time and positive-time components

$$u(\mathbf{x}', t) = G(\mathbf{x}', \mathbf{x}_A, t) + G(\mathbf{x}', \mathbf{x}_A, -t), \quad (11)$$

where $G(\mathbf{x}', \mathbf{x}_A, -t)$ represents the acausal contribution due to the wavefield propagating inwards from the sources on S to position \mathbf{x}' before refocusing at \mathbf{x}_A , and $G(\mathbf{x}', \mathbf{x}_A, t)$ represents the causal contribution due to the wavefield propagating outward from \mathbf{x}_A to \mathbf{x}' , after refocusing.

By substituting Eq. (11) for the left side of Eq. (10), applying source-receiver reciprocity (i.e. $G(\mathbf{x}, \mathbf{x}_A, t) = G(\mathbf{x}_A, \mathbf{x}, t)$) and setting $\mathbf{x}' = \mathbf{x}_B$ (the location of a receiver anywhere inside the boundary S), the following expression is obtained:

$$G(\mathbf{x}_B, \mathbf{x}_A, t) + G(\mathbf{x}_B, \mathbf{x}_A, -t) \propto \int_S G(\mathbf{x}_B, \mathbf{x}, t) * G(\mathbf{x}_A, \mathbf{x}, -t) dS. \quad (12)$$

The right-hand side of Eq. (12) gives the integral, over all boundary sources at \mathbf{x} on S , of cross-correlations of wavefield recordings obtained by receivers at \mathbf{x}_B and \mathbf{x}_A ; the left-hand side of the equation shows that the result is the superposition of the signal recorded at \mathbf{x}_B for an impulsive source located at \mathbf{x}_A and its time-reversed version (Fig. 6(c)). This reconstructed Green's function contains both the direct wave from the virtual source at \mathbf{x}_A to the receiver and all contributions due to scattering.

Although the derivation by Derode et al. (2003a, 2003b) is helpful in understanding the physical aspects of seismic interferometry, it is not mathematically precise for a general Earth-like heterogeneous medium. In the next section, exact mathematical results based on representation theorems are presented.

5.2. Interferometry and Reciprocity

The now-standard mathematical approach to prove how Green's functions are retrieved in seismic interferometry begins with the definition of a convolutional and a correlational reciprocity theorem (theorems that relate two independent acoustic or elastodynamic states, A and B, of a medium – in this case the states being differentiated by having sources at different locations). From the reciprocity theorem of the convolution type (Rayleigh, 1878; de Hoop, 1988; Fokkema and van den Berg, 1993), by choosing impulsive point sources of volume injection rate and expressing the wavefields in terms of Green's functions in both states A and B, source-receiver reciprocity can be proved in both the acoustic and the elastic case. For acoustic media this is stated as

$$G(\mathbf{x}_B, \mathbf{x}_A, \omega) = G(\mathbf{x}_A, \mathbf{x}_B, \omega) \quad (13)$$

and was actually used above in the physical argument from Derode et al. (2003a, 2003b). This expression states that the signal recorded at location \mathbf{x}_B due to a source at \mathbf{x}_A is equal to the signal recorded at location \mathbf{x}_A due to a source at \mathbf{x}_B . This result is particularly important in the case of seismic interferometry, as it allows progress from inter-receiver interferometry to both inter-source and source-receiver interferometry by variously interchanging sources and receivers – see below.

From the acoustic reciprocity theorem of the correlation type (de Hoop, 1988; Fokkema and van den Berg, 1993), Wapenaar (2004), van Manen et al. (2005, 2006) and Wapenaar and Fokkema (2006) derive exact representations of the Green's function between \mathbf{x}_A and \mathbf{x}_B . The expression obtained by Wapenaar and Fokkema (2006) is slightly different from that obtained by van Manen et al. (2005) due to a difference in the type of source assumed: Wapenaar and Fokkema (2006) assume volume injection rate density sources, while van Manen et al. (2005) assume the change in volume injection rate density over time. The *interferometric formula for acoustic waves* derived by van Manen et al. (2005) is

$$\begin{aligned} \tilde{G}^*(\mathbf{x}_B, \mathbf{x}_A) - \tilde{G}(\mathbf{x}_B, \mathbf{x}_A) \\ = \int_S \frac{1}{\rho(\mathbf{x})} \left[\left(\partial_j \tilde{G}(\mathbf{x}_B, \mathbf{x}) \right) \tilde{G}^*(\mathbf{x}_A, \mathbf{x}) - \tilde{G}(\mathbf{x}_B, \mathbf{x}) \left(\partial_j \tilde{G}^*(\mathbf{x}_A, \mathbf{x}) \right) \right] n_j dS, \end{aligned} \quad (14)$$

and by Wapenaar and Fokkema (2006) is

$$\begin{aligned} \hat{G}^*(\mathbf{x}_B, \mathbf{x}_A) + \hat{G}(\mathbf{x}_B, \mathbf{x}_A) \\ = - \int_S \frac{1}{\omega \rho(\mathbf{x})} \left[\left(\partial_j \hat{G}(\mathbf{x}_B, \mathbf{x}) \right) \hat{G}^*(\mathbf{x}_A, \mathbf{x}) - \hat{G}(\mathbf{x}_B, \mathbf{x}) \left(\partial_j \hat{G}^*(\mathbf{x}_A, \mathbf{x}) \right) \right] n_j dS \end{aligned} \quad (15)$$

where $\iota = \sqrt{-1}$, n_j is the j^{th} component of the outward-pointing normal \mathbf{n} to boundary S , $\rho(\mathbf{x})$ is the mass density of the medium at \mathbf{x} (for simplicity, we drop the \mathbf{x} -dependence in all subsequent equations), ∂_j is the partial derivative with respect to the j^{th} coordinate at the source location \mathbf{x} , dS represents integration over surface S and the different notation in the Green's function terms arises from the difference in the source types used. In both cases, the Green's functions are given in the frequency domain and the terms G and $\partial_j G$ under the integral represent the responses for monopole and dipole sources on S , respectively (since the latter results in a spatial derivative over the source coordinates taken in the direction perpendicular to the outer boundary of sources). Dipolar or coupled sources are familiar to tectonophysicists as earthquake source mechanisms are usually represented as a double-couple, or a pair of dipoles. The products in the integral correspond to cross-correlations in the time domain.

Eqs. (14) and (15) provide exact representations of the Green's function between \mathbf{x}_A and \mathbf{x}_B . Also, unlike the time-reversal approach

in Eq. (12), no assumption is made regarding the homogeneity of the medium outside of boundary S (made by Derode et al., 2003a, 2003b) to ensure no waves entered the medium through surface S ; instead, in Eqs. (14) and (15) the combination of products of Green's functions for monopole and dipole sources ensures that there is no interaction between waves propagating outwards and inwards through surface S .

Wapenaar et al. (2005) show that if we assume the medium outside S is homogeneous and we approximate $n_j \partial_j \hat{G}$ by $-\iota(\omega/c) \hat{G}$ (where c is the propagation velocity in the homogeneous medium), Eq. (15) becomes

$$2\Re \left\{ \hat{G}(\mathbf{x}_B, \mathbf{x}_A) \right\} \approx \frac{2}{\rho c} \int_S \hat{G}(\mathbf{x}_B, \mathbf{x}) \hat{G}^*(\mathbf{x}_A, \mathbf{x}) dS \quad (16)$$

When converted back into the time domain, this yields Eq. (12) with proportionality factor $2/\rho c$. Hence, the expression obtained from the time-reversal approach by Derode et al. (2003a, 2003b) can be considered an approximation of the expression obtained from the reciprocity theorem approach.

From the elastodynamic reciprocity theorem of the correlation type, Wapenaar (2004), Wapenaar and Fokkema (2006) and van Manen et al. (2006) derive expressions for the Green's function between two receivers located at \mathbf{x}_A and \mathbf{x}_B in an *elastic* medium. Similarly to the acoustic case, the expressions derived by Wapenaar (2004) and Wapenaar and Fokkema (2006), and by van Manen et al. (2006) present some differences which are due to the different source terms and quantities recorded. van Manen et al. (2006) derive the following interferometric formula for elastodynamic waves:

$$\begin{aligned} \tilde{G}_{im}^*(\mathbf{x}_B, \mathbf{x}_A) - \tilde{G}_{im}(\mathbf{x}_B, \mathbf{x}_A) \\ = - \int_S c_{ijkl}(\mathbf{x}) \left[\left(\partial_k \tilde{G}_{il}(\mathbf{x}_B, \mathbf{x}) \right) \tilde{G}_{mn}^*(\mathbf{x}_A, \mathbf{x}) - \tilde{G}_{im}(\mathbf{x}_B, \mathbf{x}) \left(\partial_k \tilde{G}_{ml}^*(\mathbf{x}_A, \mathbf{x}) \right) \right] n_j dS, \end{aligned} \quad (17)$$

where $c_{ijkl}(\mathbf{x})$ is the stiffness tensor at \mathbf{x} (for simplicity, we drop the \mathbf{x} -dependence in all subsequent equations), ∂_k denotes the partial derivative in the k -direction with respect to the source location \mathbf{x} , and $\tilde{G}_{im}(\mathbf{x}_B, \mathbf{x}_A)$ represents the *displacement* Green's function at location \mathbf{x}_B in the i -direction due to a uni-directional point force in the m -direction at location \mathbf{x}_A . Wapenaar (2004) and Wapenaar and Fokkema (2006) instead find

$$\begin{aligned} \hat{G}_{qp}^*(\mathbf{x}_B, \mathbf{x}_A) + \hat{G}_{qp}(\mathbf{x}_B, \mathbf{x}_A) \\ = - \int_S \frac{c_{ijkl}}{\omega} \left[\left(\partial_l \hat{G}_{qk}(\mathbf{x}_B, \mathbf{x}) \right) \hat{G}_{pi}^*(\mathbf{x}_A, \mathbf{x}) - \hat{G}_{qi}(\mathbf{x}_B, \mathbf{x}) \left(\partial_l \hat{G}_{pk}^*(\mathbf{x}_A, \mathbf{x}) \right) \right] n_j dS, \end{aligned} \quad (18)$$

where $\hat{G}_{qp}(\mathbf{x}_B, \mathbf{x}_A)$ represents the *particle velocity* Green's function at location \mathbf{x}_B in the q -direction due to an impulsive point force excitation rate in the p -direction at location \mathbf{x}_A . The terms $\hat{G}_{pi}(\mathbf{x}_A, \mathbf{x})$ and $(c_{ijkl}/\omega) \partial_l \hat{G}_{pk}(\mathbf{x}_A, \mathbf{x}) n_j$ under the integral represent the p^{th} component of particle velocity observed at \mathbf{x}_A due to respectively volume force and deformation rate tensor sources at \mathbf{x} . Both expressions are given in the frequency domain and Einstein's summation convention for repeated indices applies.

Eqs. (17) and (18) provide exact representations of the elastodynamic Green's function between locations \mathbf{x}_A and \mathbf{x}_B as though a source had been fired at location \mathbf{x}_A , using only recordings of sources fired on the boundary. Thus, the receiver at location \mathbf{x}_A is turned into a virtual source. Similarly to the acoustic case, these equations can be simplified by making a number of assumptions (e.g. homogeneous medium outside S) or approximations (e.g., a source boundary S that is far from the receiver pair) which result in a single correlation

operation and remove the need for dipole sources in the integrand, similar to Eq. (16) (Wapenaar and Fokkema, 2006).

If noise sources are to be used, Wapenaar and Fokkema (2006) show that if noise sources distributed around the boundary S are uncorrelated, the approximate Green's function between \mathbf{x}_A and \mathbf{x}_B in the acoustic case is obtained from the above expressions by

$$2\Re\{\widehat{G}(\mathbf{x}_B, \mathbf{x}_A, \omega)\} S(\omega) \approx \frac{2}{\rho c} \langle p^{obs}(\mathbf{x}_B, \omega) p^{obs*}(\mathbf{x}_A, \omega) \rangle, \quad (19)$$

where $S(\omega)$ is the power spectrum of the noise, $p^{obs}(\mathbf{x}_A, \omega)$ and $p^{obs}(\mathbf{x}_B, \omega)$ indicate the observed noise wavefields at \mathbf{x}_A and \mathbf{x}_B , and $\langle \cdot \rangle$ denotes spatial ensemble average. This shows precisely how the Green's functions between \mathbf{x}_A and \mathbf{x}_B is approximated by cross-correlation of recordings of ambient noise at each of the receiver locations. Similar expressions exist for elastic media.

5.3. Stationary-Phase Approach

Analysing seismic interferometry using the method of stationary phase is particularly useful to understand the mechanisms of constructive and destructive interference that account for the emergence of the Green's function from the above cross-correlations of wavefields (Snieder, 2004; Snieder et al., 2006). Snieder et al. (2006) consider a model consisting of a single horizontal reflector with reflection coefficient r for downward-travelling waves, embedded in a homogeneous medium. The sources, located on the free surface at $\mathbf{r} = (x, y, 0)$, with a density of n sources per unit area, are assumed to be uncorrelated, and receivers are located within the Earth at locations $\mathbf{r}_A = (x_A, 0, z_A)$ and $\mathbf{r}_B = (x_B, 0, z_B)$, as shown in Fig. 7(a). The cross-correlation of wavefields recorded at the two receivers in the frequency domain is given by

$$C_{AB}(\omega) = |S(\omega)|^2 n \int_{\mathbf{r}} G^{full}(\mathbf{r}_B, \mathbf{r}) G^{full*}(\mathbf{r}_A, \mathbf{r}) dx dy, \quad (20)$$

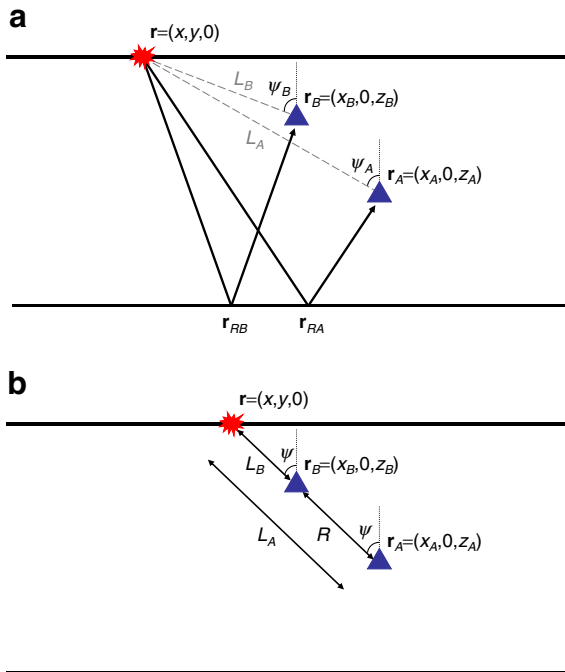


Fig. 7. Geometry of a simple model and raypaths for a derivation of seismic interferometry based on stationary phase. (a) A source is located on the surface at \mathbf{r} and two receivers are located in the subsurface at \mathbf{r}_A and \mathbf{r}_B . Reflection points are located at \mathbf{r}_{RA} and \mathbf{r}_{RB} . The variables used in the analysis of term T1 are also defined. (b) The stationary source in term T1 is located along the line joining the two receivers. Redrawn after Snieder et al. (2006).

where $|S(\omega)|^2$ is the power spectrum of the sources, and G^{full} denotes the full Green's function consisting of the direct and singly-reflected wave in the frequency domain. The full Green's functions recorded at each of the two receivers are given by

$$G^{full}(\mathbf{r}_A, \mathbf{r}) = G(|\mathbf{r}_A - \mathbf{r}|) + rG(|\mathbf{r}_A - \mathbf{r}_{RA}| + |\mathbf{r}_{RA} - \mathbf{r}|) \quad (21a)$$

and

$$G^{full}(\mathbf{r}_B, \mathbf{r}) = G(|\mathbf{r}_B - \mathbf{r}|) + rG(|\mathbf{r}_B - \mathbf{r}_{RB}| + |\mathbf{r}_{RB} - \mathbf{r}|) \quad (21b)$$

where, on the right-hand side of both equations, the first term represents the direct wave and the second term represents the singly reflected wave. By inserting Eqs. (21a) and (21b) into Eq. (20), an expression consisting of the sum of four terms is obtained: term T1 is the correlation of direct waves to both receivers; terms T2 and T3 are given by the correlation of a direct and a reflected wave to the receivers; term T4 is the correlation of reflected waves to both receivers. All four terms contain the Green's function for a homogeneous medium

$$G(R) = -\rho \frac{\exp(-ikR)}{4\pi R}, \quad (22)$$

where R is the distance of propagation between the source and one receiver, which contains an oscillatory integrand of the form $\exp(-ikR)$, and this term has a stationary point that depends on the expression for R in Eqs. (21a) and (21b). For this reason, in all four terms the integral is analysed in the stationary-phase approximation. This assumes that the amplitude of the integral varies smoothly compared to the phase, in which case the dominant contributions to the integral in Eq. (20) come from points \mathbf{r} where the phase is stationary (becomes constant) with respect to the boundary source position. As an example, consider term T1:

$$T1 = \int G(|\mathbf{r}_B - \mathbf{r}|) G^*(|\mathbf{r}_A - \mathbf{r}|) dx dy = \frac{\rho^2}{(4\pi)^2} \int \frac{\exp(-ik(L_A - L_B))}{L_A L_B} dx dy, \quad (23)$$

where quantities L_A and L_B are defined in Fig. 7(a). Snieder et al. (2006) show that the phase of the integrand is stationary when $\psi_A = \psi_B$ and $y = 0$, where the angles ψ_A and ψ_B are also defined in Fig. 7(a). This corresponds to a source located along the line of the receivers, as shown in Fig. 7(b).

Snieder et al. (2006) repeat the analysis for terms T2, T3, T4 and determine the locations of the stationary points for each term. The source positions and ray paths corresponding to the stationary contributions in the integrals are shown in Fig. 8: energy travelling along the ray paths in (a) contribute to the causal and acausal direct waves, propagating directly between the two receivers; the ray paths in panel (b) contribute to the causal and acausal singly-reflected waves, which propagate between the two receivers via a reflection at the interface. In all four cases, the sources corresponding to the stationary points are located along the extension of the ray path joining the two receivers (in the case of reflected waves, the mirror images below the reflectors can be considered). Hence, as the phase of the correlation is stationary only for the raypaths that are aligned with the inter-receiver line, it follows that the main contribution to the Green's function emergence is given by sources at or around those that contribute to these paths, for which energy passes and is recorded by both receivers; signals resulting from sources on other ray paths interfere destructively upon integration over all the sources, due to the oscillation of the exponential in Eq. (23).

Snieder (2004) shows in a 2D model that this latter statement is also true for waves in the scattered coda in the approach of Campillo and Paul (2003): those that pass the locations of both

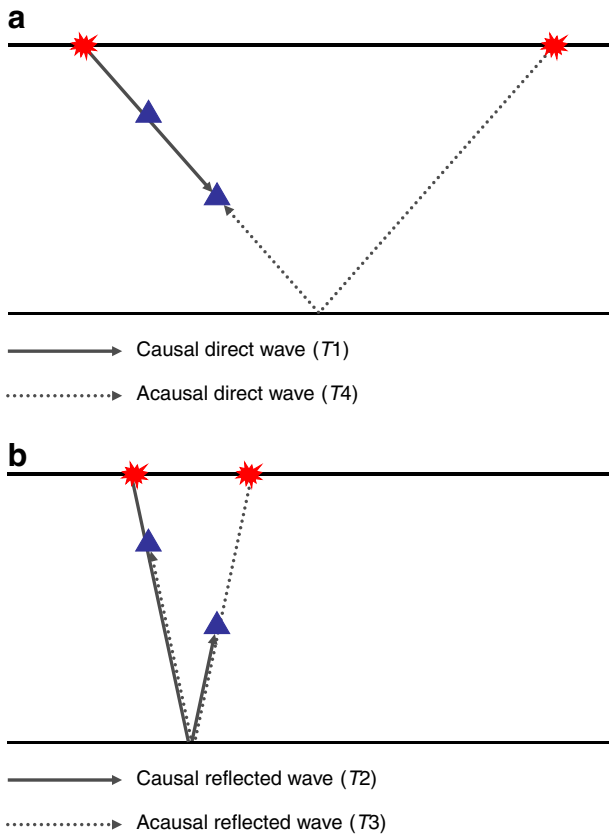


Fig. 8. Raypaths corresponding to the four terms resulting from the cross-correlation of the full wavefields recorded at the two receivers: (a) causal direct wave from term T1 and acausal direct wave from term T4; (b) causal reflected wave from term T2 and acausal reflected wave from term T3. Redrawn after Snieder et al. (2006).

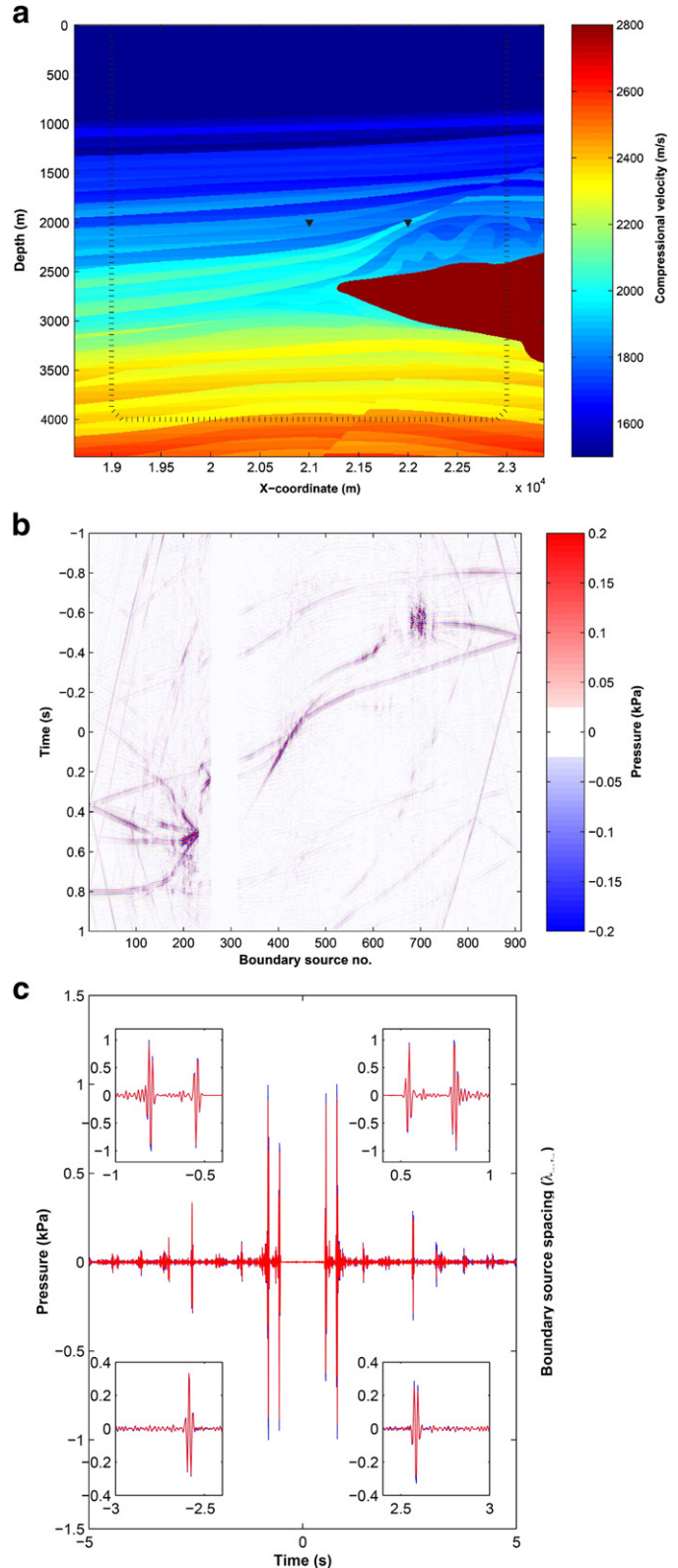
receivers contribute energy that is stationary in the above sense, and hence which survives the cross-correlation process. In 3D media, Halliday and Curtis (2008) show that subsurface point sources are also necessary (even for surface waves) in order to excite all stationary-phase points and hence produce correct interferometric reconstructions.

Snieder et al. (2006) show that in the stationary-phase analysis for a medium with more than one reflector, if sources are only present on the surface the cross-terms of wavefields resulting from reflections at different reflectors may give non-zero contributions that are proportional to the product of the reflection coefficients at the reflecting interfaces. These signals, which do not correspond to physical events and would vanish in the presence of a closed boundary of sources, are therefore named *spurious multiples*. A development of the discussion of spurious multiples and their use in exploration seismology is provided by Halliday and Curtis (2009b) and King et al. (2011)

Fig. 9. Model and simulation results from van Manen et al. (2005). (a) 2D acoustic marine seismic model including a high-velocity salt body. The boundary of 912 sources is represented by the dotted line; the two receivers are represented by the triangles. (b) Correlation gather for the two receivers shown in (a). (c) Comparison between the waveform obtained by stacking (summing) all traces from the correlation gather in (b) (red line) and that obtained from direct forward modelling (blue line). Reprinted figure with permission from van Manen, D.-J., Robertsson, J.O.A., Curtis, A., *Physical Review Letters* 94 (16), 164301, 2005. Copyright (2005) by the American Physical Society (<http://prl.aps.org/abstract/PRL/v94/i16/e164301>). Readers may view, browse, and/or download material for temporary copying purposes only, provided these uses are for noncommercial personal purposes. Except as provided by law, this material may not be further reproduced, distributed, transmitted, modified, adapted, performed, displayed, published, or sold in whole or part, without prior written permission from the American Physical Society.

(see next section), where the more general term *non-physical* contributions is used in place of spurious multiples.

An example of how Green's functions emerge from waves with stationary phase in more complex media is given by van Manen



et al. (2005). Their 2D acoustic seismic model, which includes a salt dome, is shown in Fig. 9(a). Sources are located along the dotted line and receivers are represented by the two triangles. Wave-propagation simulations are carried out for each source separately and the cross-correlations of the resulting traces recorded at the two receivers are shown in Fig. 9(b) for each source. When these traces are stacked (summed), the seismogram represented in Fig. 9(c) is obtained: the points in plot (b) that are stationary with respect to source position (identified as waves lying on horizontal lines in plot (b)) provide the dominant contributions, and the Green's function between the two receivers (red) emerges here as a result of constructive and destructive interference between the wavefields propagating through the medium from each source. This trace perfectly matches the reference trace obtained by direct forward modelling (blue).

Halliday and Curtis (2009b) repeat the stationary-phase analysis for scattered (rather than reflected) waves and include the effects of attenuation. Similarly to Snieder (2004) and Snieder et al. (2006), four different contributions (T_1 , T_2 , T_3 , T_4) to the interferometric integral are obtained, defined similarly to above, and are analysed for the

stationary-phase contributions. The analysis yields similar results to the study by Snieder (2004), and the stationary source points for T_1 are found to be those aligned with the inter-receiver line. Assuming a closed source boundary, terms T_2 and T_3 contribute both physical and non-physical parts (Fig. 10) the non-physical parts of which are cancelled by term T_4 when no attenuation is present.

In the case of attenuative media (like the real Earth), this complete cancellation does not occur since contributions T_2 , T_3 and T_4 may be differentially attenuated. This results in spurious or non-physical arrivals in the reconstructed seismograms. Slob et al. (2007) and Halliday and Curtis (2009b) show that this difficulty can be overcome by using seismic interferometry by convolution instead of correlation. This technique was developed by Slob et al. (2007) for electromagnetic waves which are often affected by strong attenuation. The interferometric relationship of convolution type is derived from the reciprocity theorem of the convolution type and importantly requires one of the receivers to be outside of the boundary of sources (e.g. compare Fig. 11(a) for correlation and Fig. 11(b) for convolution). This relationship only provides the causal component of the Green's function and for (an)elastic media is given in the frequency domain by the following equation:

$$\tilde{G}_{im}(\mathbf{x}_B, \mathbf{x}_A) = \int_S c_{njkl} \left[\tilde{G}_{in}(\mathbf{x}_B, \mathbf{x}) (\partial_k \tilde{G}_{ml}(\mathbf{x}_A, \mathbf{x})) - (\partial_k \tilde{G}_{il}(\mathbf{x}_B, \mathbf{x})) \tilde{G}_{mn}(\mathbf{x}_A, \mathbf{x}) \right] n_j dS, \quad (24)$$

where ∂_k acts on the source coordinate \mathbf{x} and only one of \mathbf{x}_A and \mathbf{x}_B is inside the boundary of sources S . Examples of stationary-phase analysis for scattered surface waves are shown in Fig. 11, where the solid and dashed lines indicate the interferometric and the directly modelled waveforms, respectively. In (c), the sum of the four terms T_1 - T_4 for the model shown in (a) and no attenuation is shown when correlational interferometry is used as in Eqs. (14), (15), (17), (18). In this case, no non-physical arrivals are present, as the non-physical contributions brought by T_2 , T_3 and T_4 mutually cancel. In contrast, a non-physical event and strong amplitude distortions are visible in (d), which displays the sum of the four terms for the same model as (c) but with the effects of attenuation included. Instead, if convolution, rather than cross-correlation, is applied for case (b), the waveform shown in (e) is obtained: despite the amplitude mismatch in the early, low-frequency arrivals caused by the absence of sources at depth, this signal only contains a causal part and presents no non-physical arrivals. Convolutional interferometry is therefore likely to be more suitable for near surface applications, where complex scattering and attenuation are likely to occur, provided an appropriate source geometry exists. However, the convolutional method only works for transient sources, hence it is not applicable in the case of ambient noise.

Halliday and Curtis (2008) use the stationary-phase approach to analyse the effect of source distribution on the construction of surface wave signals from seismic interferometry (the most common application of seismic interferometry). One of their most striking findings is that, contrarily to common opinion, sources at depth also play an important role in the interferometric construction of surface waves. In fact, the use of deep sources allows the correct amplitudes to be recovered for all surface wave modes without the introduction of spurious or non-physical events which otherwise result from the cross-correlation of different modes with each other (so-called modal cross-talk). If an ideal source distribution is not available, modal separation prior to cross-correlation is found to provide correct estimates of the wavefield propagating between the receivers in some practical geometries.

The discussion of physical and non-physical energy is complex but is extremely important. It explains why in practice the Green's function estimates from virtual sources derived using seismic interferometry do not necessarily look exactly like seismograms that would be recorded from real sources, and how and why they differ.

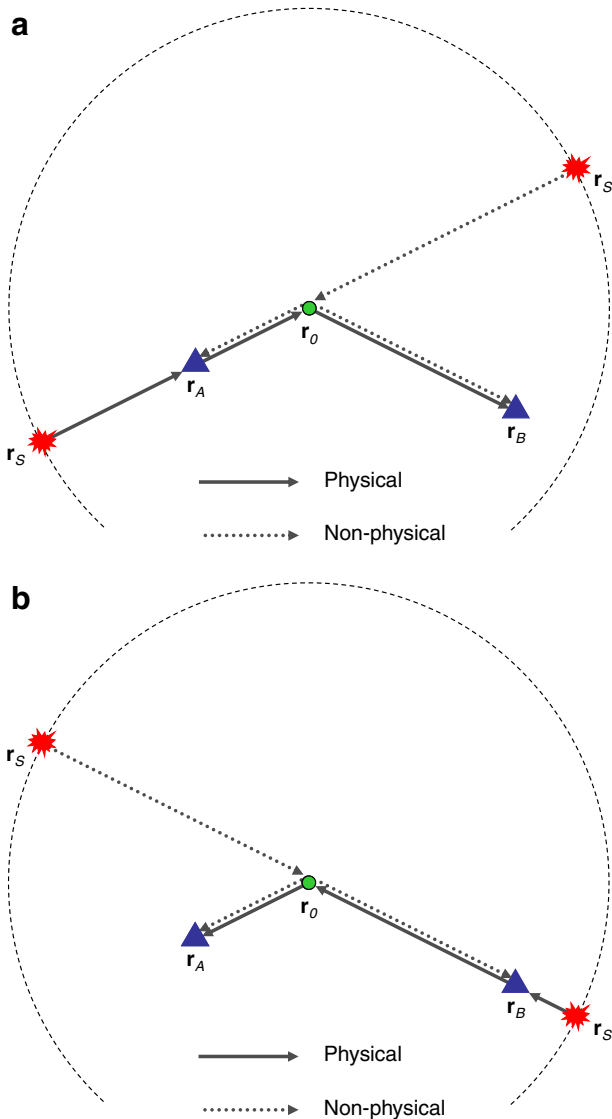


Fig. 10. Stationary source points (\mathbf{r}_S) in the interferometric integral for wave propagation from receiver \mathbf{r}_A to receiver \mathbf{r}_B , with a scatterer at location \mathbf{r}_0 . The boundary of sources is indicated by a dashed line. (a) Physical and non-physical part of term T_2 ; (b) physical and non-physical part of term T_3 .

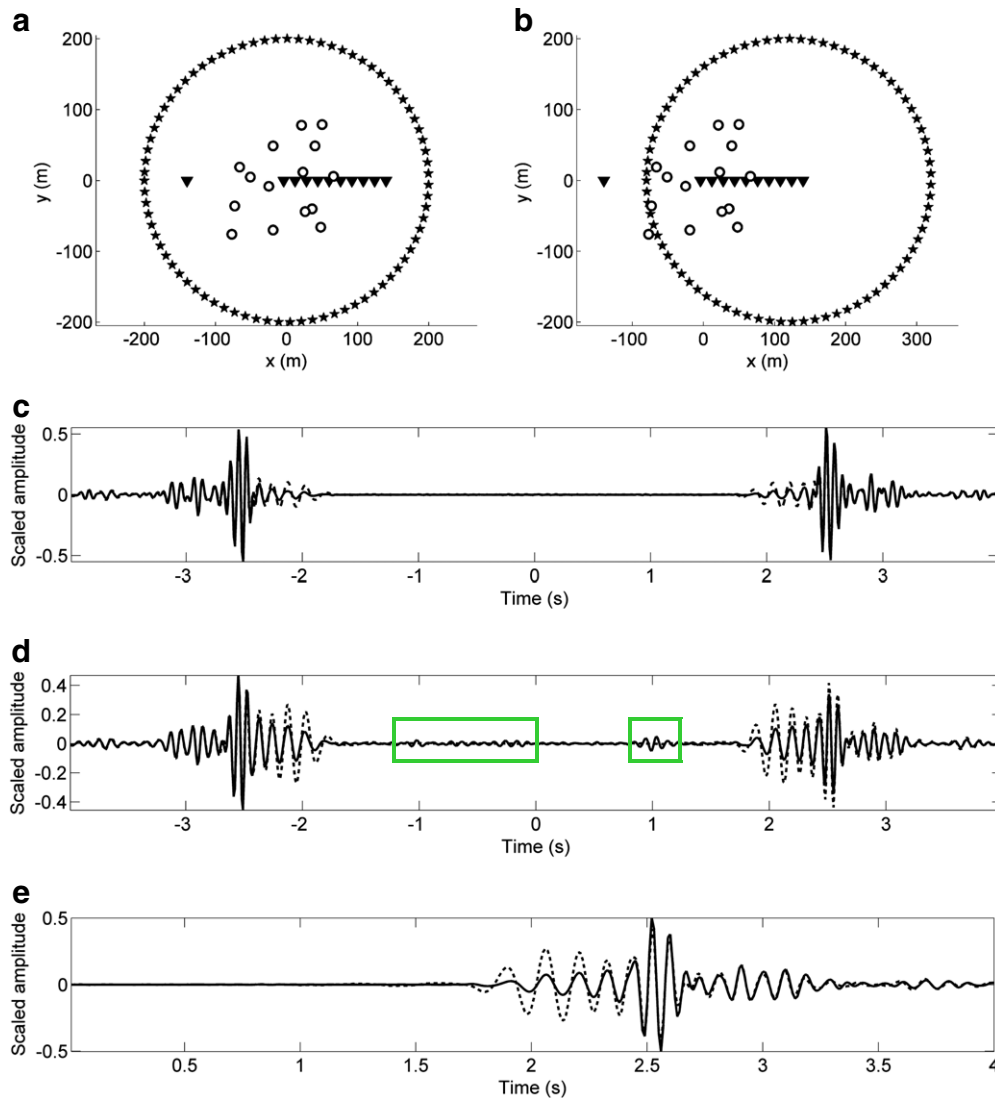


Fig. 11. Comparison between waveforms obtained by summing the four contributions to the interferometric integral (solid lines) and those obtained from direct modelling (dashed lines) for scattered surface waves, in the case of the two models shown in (a) and (b), where triangles represent receivers, stars represent sources and circles indicate scatterers. (c) Waveform for model (a) with no attenuation; (d) waveform for model (a) with attenuation. Green boxes highlight non-physical arrivals. (e) Waveform for model (b) with attenuation. From Halliday, D., Curtis, A., 2009. Seismic interferometry of scattered surface waves in attenuative media. *Geophys. J. Int.* 178 (1), 419–446. Reprinted with permission from John Wiley & Sons Ltd.

Nevertheless, it should not be assumed that non-physical energy is always unwanted; on the contrary, since it is also formed by combining (e.g. cross-correlating) recorded, physically-propagating energy, it also contains information about the medium (the Earth). For example, King et al. (2011) use non-physical energy to retrieve information about subsurface layer velocities and thicknesses, as described in the next section. Mikesell et al. (2009) also use energy in the non-physical, so-called “virtual refraction” for the same purpose. It is currently a moot point as to whether physical or non-physical energy contains most information about the medium.

Despite being the most popular and widely used form of seismic interferometry, cross-correlational interferometry presents several limitations (Curtis and Halliday, 2010b; Halliday and Curtis, 2008; 2009b; Slob and Wapenaar, 2007; Stehly et al., 2008; Harmon et al., 2010). It provides reasonably accurate Green’s function estimates when the medium is lossless and the waves are equipartitioned (e.g., if the distribution of sources is regular around the receivers and the sources are transient or uncorrelated with equal autocorrelation functions and power spectra), but these assumptions seldom hold in practical applications, causing the Green’s function estimate to be affected by non-physical artifacts. In addition, the Green’s

function retrieved from cross-correlation when these assumptions are not satisfied is proportional to the Green’s function that would be generated by a spatio-temporally blurred source, the distortion being quantified by a so-called point-spread function (Wapenaar and van der Neut, 2010).

By replacing the cross-correlation operation with deconvolution (see Eq. (1)), Vasconcelos and Snieder (2008a, 2008b) showed how these assumptions may be avoided and a more accurate representation of the Green’s function may be obtained. Similarly, in their so-called *directional balancing* method, Curtis and Halliday (2010b) used deconvolution to reduce the effects that an irregular distribution of sources may have on the Green’s functions retrieved by cross-correlation. What is more, interferometry by deconvolution may be extended to two or three dimensions, giving rise to the method of multi-dimensional deconvolution (MDD) (Wapenaar et al., 2008; Minato et al., 2011; Wapenaar et al., 2011). The main advantages of MDD over cross-correlation include the fact that the assumption of a lossless medium is relaxed, the source is deblurred to some extent, and its signature is eliminated. On the other hand, MDD requires the inversion of a matrix and a network of receivers (rather than only a single pair of receivers as in cross-correlation), and is therefore

more expensive than cross-correlational interferometry. Overall, interferometry by convolution, cross-correlation, deconvolution and multi-dimensional deconvolution present advantages and disadvantages, and one method may be preferable to another for a specific application. A detailed comparison of the latter three methods is given by Snieder et al. (2009).

6. Applications of inter-receiver interferometry

The applications of seismic interferometry span a number of different fields, including crustal seismology, volcano monitoring and industrial exploration. Almost all of these applications take advantage of the fact that inter-receiver interferometry allows real receivers to be converted into virtual sources, hence increasing the number of available sources and possible source-receiver paths.

However, the first examples of Green's function reconstruction from the cross-correlation of diffuse wavefields on Earth were obtained from laboratory experiments using ultrasonic and thermal noise (Lobkis and Weaver, 2001; Weaver and Lobkis, 2001), rather than from seismograms recorded in the natural environment. It was not until 2003 that Campillo and Paul (2003) showed that in the real Earth the Green's function between a pair of receivers can be reconstructed by cross-correlating coda wave signals from an earthquake recorded at the two receivers. Seismic codas are those parts of the seismic signal that emerge after the direct arrivals, as a result of (multiple) scattering of the waves in the subsurface. Since the location of earthquakes on the Earth's surface is inhomogeneous, it may be thanks to the presence of scatterers that wavefields originating from earthquakes become sufficiently diffuse for interferometry to work in practice. By cross-correlating seismic codas of distant earthquakes recorded at a number of seismic stations in Mexico, Campillo and Paul (2003) succeeded in reconstructing the Green's function between various station pairs. These Green's functions displayed both Rayleigh and Love wave signals and were found to agree well with theoretical Green's functions computed along the same paths using a three-layer crustal model.

Stehly et al. (2008) developed a technique for Green's function retrieval using correlation of seismic codas obtained in turn by the correlation of seismic ambient noise records. This method can be explained by considering the configuration shown in Fig. 12, where R_1 and R_2 are the receivers between which the Green's function is to be calculated. Traditionally, inter-receiver interferometry allows the Green's function between these two receivers to be computed by cross-correlating long records of ambient noise obtained at the two stations. However, although they generally provide a good estimate of the Green's function, the resulting cross-correlations are usually not perfect due to an inhomogeneous distribution of noise sources. In fact, the reconstructed Green's functions may present

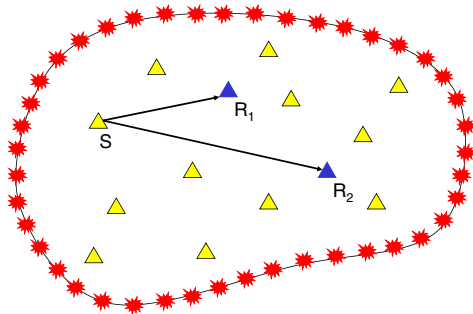


Fig. 12. Schematic representation of the geometry used in the C^3 method developed by Stehly et al. (2008). A boundary of seismic noise sources encloses a network of receivers. The Green's function between the blue receivers R_1 and R_2 is reconstructed by cross-correlating the codas of the Green's functions obtained from cross-correlation of noise records from these receivers and all the yellow receivers S in the network.

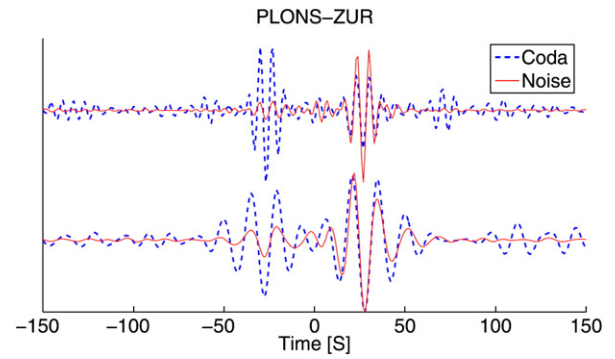
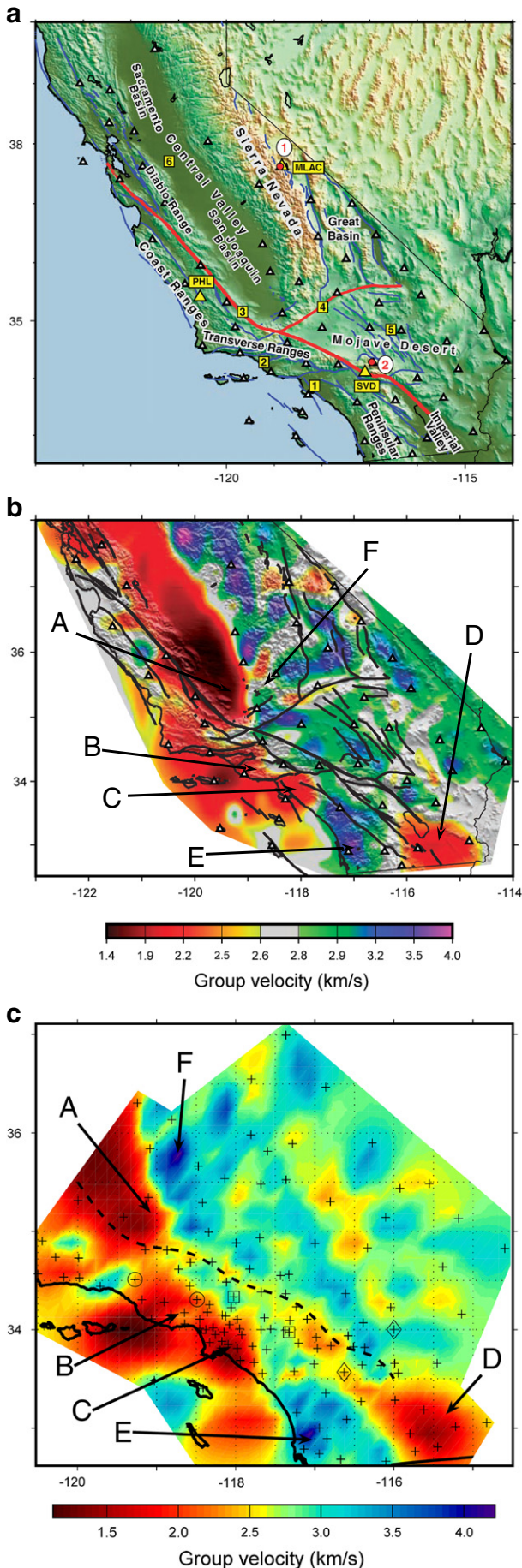


Fig. 13. Comparison of Green's functions obtained from noise cross-correlation (solid red line) and the C^3 method (dashed blue line) in the period bands of 5–10 s (top) and 10–20 s (bottom). Reprinted from Stehly et al. (2008).

spurious or non-physical arrivals due to incomplete cancellation upon stacking, and may also be asymmetric between positive and negative times due to the presence of directionality in the noise field. Hence, rather than cross-correlating passive noise or real codas recorded at R_1 and R_2 , Stehly et al. (2008) start by computing ambient noise correlations between each of these two stations and a third station S that is varied around a neighbouring station network. The resulting seismograms correspond to those that would be recorded at R_1 and R_2 if a source had been placed at S . For each seismogram from such a receiver S , they then select the time window corresponding to the coda (at positive and negative time) of the Green's function recorded at R_1 and R_2 for a virtual source at S , and compute four cross-correlations (positive-positive, negative-negative, positive-negative, negative-positive times). Finally, these intermediate cross-correlations are separately averaged over all stations S in the network and stacked to obtain the so-called C^3 (Correlation of Coda of Correlation) function.

An example of the application of this technique to records obtained at stations PLONS and ZUR in the Swiss Alps is shown in Fig. 13. In this case, since the intermediate positive-negative and negative-positive cross-correlations had a very low signal-to-noise ratio which would not greatly improve the reconstruction of the Green's function, the C^3 function was calculated by stacking only the coda wave correlations for positive and negative times. For both the 5–10 s period band (top) and the 10–20 s period band (bottom), the C^3 functions present Rayleigh wave arrivals that match those obtained by simply cross-correlating noise records from the two stations. However, the Green's function reconstructed from noise correlations is not symmetric and has a relatively low signal-to-noise ratio, and it would not normally be used in tomography studies. In contrast, the C^3 function is symmetric, and could therefore be used more reliably when performing surface wave tomography. In fact, while the amplitude of noise correlations depends on the distribution of the sources, the azimuthal dependence is eliminated when computing the C^3 function, as the use of coda waves compensates for an anisotropic source distribution. Therefore, Stehly et al. (2008) suggest that this new method has the potential to increase the number of paths contributing to Rayleigh wave tomography, improving the resolution of crustal models.

Since the work of Campillo and Paul (2003) surface wave ambient noise tomography has become common practice. Green's functions are reconstructed from the cross-correlation of ambient noise records (assumed to be diffuse, or coming from an approximately complete boundary of noise sources) for as many inter-receiver paths as possible within a network of receivers. From the resulting cross-correlograms, the surface wave (Rayleigh or Love) group or phase velocities are obtained at different frequencies and used to perform surface wave tomography. As different frequencies are sensitive to seismic velocities at different depths in the Earth (generally



higher frequencies oscillate in shallower layers, lower frequencies in deeper layers), it is possible to construct velocity models of the subsurface at a range of depths that depends on the set of frequencies considered. Since in principle this method does not depend on source location but only on the location of the receivers, it is particularly useful in aseismic regions where traditional tomography using teleseismic earthquake sources is not able to provide sufficiently high resolution.

In 2005 both Shapiro et al. (2005) and Sabra et al. (2005) produced velocity maps of California which agreed well with the known regional geology (e.g., Fig. 14) using the correlational method. Ambient noise surface wave tomography has since been applied successfully to Europe (Yang et al., 2007), the Iberian Peninsula (Villaseñor et al., 2007), Iceland (Gudmundsson et al., 2007), Italy (Li et al., 2010a), Australia (Rawlinson et al., 2008; Arroucau et al., 2010; Saygin and Kennett, 2010), New Zealand (Lin et al., 2007), South Africa (Yang et al., 2008), China (Zheng et al., 2008; Li et al., 2009; Zheng et al., 2010), South Korea (Cho et al., 2007), the United States (Bensen et al., 2008; Liang and Langston, 2008; Lin et al., 2008), the Tibetan Plateau (Yao et al., 2006; Yao et al., 2008; Li et al., 2009; Li et al., 2010b), the Alps (Stehly et al., 2009) and Scotland (Nicolson et al., 2012). In addition, by performing surface wave ambient noise tomography at the Piton de la Fournaise volcano, Brenguier et al. (2007) showed that this technique can be used to image volcanic edifices.

In industrial exploration, some of the first applications of seismic interferometry were to perform seismic imaging and redatuming of sources to the positions of receivers. Schuster (2001) and Schuster et al. (2004) showed that by cross-correlating traces recorded in the configuration in Fig. 15(a) from either source, that data could be redatumed to the case where a virtual source was at the location of receiver R_1 and the resulting trace could be migrated to find the location of the reflector. They also explained how the data from a source in the lower layer as in Fig. 15(b) could either provide a receiver function by cross-correlating S and P waves at R_1 and R_2 which can then be used to image the reflector, or by cross-correlating P waves at each receiver the resulting time series can be used to image the source. Schuster et al. (2004) also apply interferometric imaging to a number of case studies and show how this method has the potential to image reflectivity distribution and source location from passive seismic data, without knowing either the approximate source location or source wavelet.

Surface wave retrieval from seismic interferometry has also proved useful in industrial exploration settings, where ground-roll (the industrial term for surface waves) often negatively impacts the quality of acquired seismic data. In industrial settings, ground-roll travels within the shallowest layers of the Earth and hence contains no relevant information about deeper layers. Significantly, due to its high amplitude, ground-roll often masks the deeper-reflecting arrivals which are of interest in seismic exploration. While ground roll propagating directly from the source to a receiver is relatively easy to remove using standard frequency-wavenumber (f - k) filters, scattered ground roll (surface waves that have scattered from heterogeneities in the subsurface) is particularly difficult to remove because it may occupy the same part of f - k space as the body wave reflections or refractions of interest.

Fig. 14. (a) Reference map of California. Group-velocity maps obtained from ambient noise tomography by (b) Shapiro et al. (2005) and (c) Sabra et al. (2005). In (a) the yellow squares with digits indicate the following features: (1) Los Angeles Basin, (2) Ventura Basin, (3) San Andreas Fault, (4) Garlock Fault, (5) Mojave shear zone, and (6) Stockton Arch. In (b) and (c) the letters indicate the following features: (A) San Joaquin Valley, (B) Ventura basin, (C) Los Angeles basin, (D) Salton Sea, (E) Peninsular Ranges, (F) Sierra Nevada. (a) and (b) from Shapiro, N.M., Campillo, M., Stehly, L., Ritzwoller, M.H., 2005. High-Resolution Surface-Wave Tomography from Ambient Seismic Noise. *Science*, 307 (5715), 1615–1618. Reprinted with permission from AAAS. (c) Modified with permission from Sabra et al. (2005).

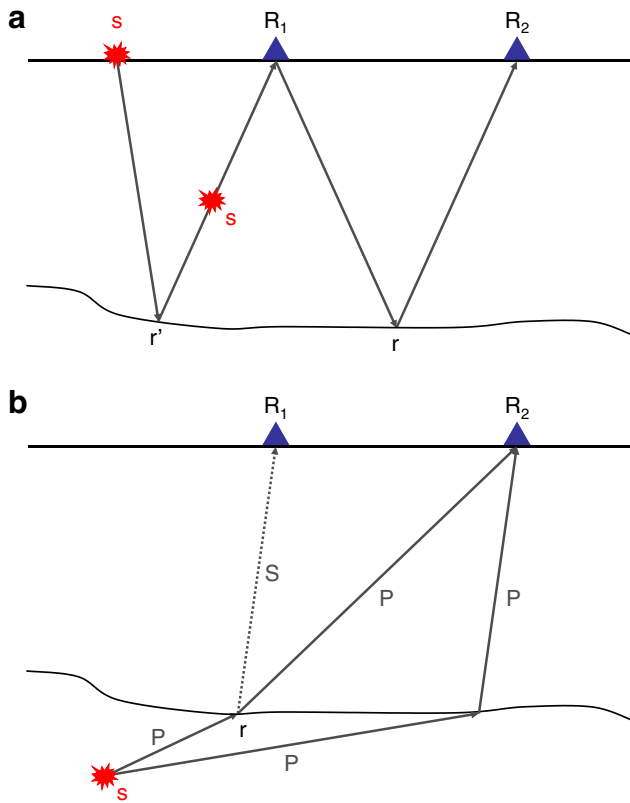


Fig. 15. Different geometries for cross-correlation in interferometric/daylight seismic imaging: (a) cross-correlation of data recorded at receivers R_1 and R_2 from either source gives the trace that would be recorded at R_2 if a source were placed at R_1 ; (b) cross-correlation of data from a source in the lower layer can be used to image either the reflector or the source. Redrawn after Schuster et al. (2004).

Curtis et al. (2006), Dong et al. (2006), and Halliday et al. (2007, 2010a) use cross-correlational and convolutional interferometry to predict scattered surface waves between receiver locations within an industrial seismic data set. For sources with neighbouring

receiver locations this prediction may be adaptively subtracted from real-source to receiver records, leaving the body wave energy untouched. Their method allows better quality data to be obtained, as it successfully attenuates the effects of ground-roll while preserving the reflection signals. An example of this technique is given in Fig. 16 (Halliday, 2010): the scattered surface waves predicted from seismic interferometry are shown in (b); these signals, after being adaptively filtered, are subtracted from the raw data in (a), giving the cleaner data set shown in (c) in which body waves are clearly visible.

However, the application of seismic interferometry in the industrial domain is not restricted to the removal of surface waves. From the principles of time-reversed acoustics, Bakulin and Calvert (2004, 2006) developed a method that allowed them to image below the complex surface overburden by turning real downhole receivers into virtual sources. Their so-called *virtual source method* (VSM) is illustrated in Fig. 17: by cross-correlating the signals recorded at two different downhole receivers in a near-horizontal well, one of the receivers is turned into a virtual source, whose signal is recorded at the other receiver. Hence, many of the distortions caused by the complex near-surface are eliminated, providing much cleaner and distortion-free data, without any knowledge of the complex overburden.

Mehta et al. (2007) show that this method can be improved significantly by cross-correlating wavefields that have been decomposed into up- and down-going components prior to interferometry. Correlating the downwards-propagating field at one location with the upwards-propagating part at another location eliminates many of the non-physical arrivals that otherwise occur. Bakulin et al. (2007) and Mehta et al. (2008) suggest how the VSM may also be used as a time-dependent reservoir monitoring technique thanks to its ability to eliminate the effect of temporal variations in the overburden.

Another application of inter-receiver interferometry in exploration settings is the method of *interferometric velocity analysis* (King et al., 2011), which allows layer velocity and thickness to be retrieved using non-physical as well as physical energy. The method is presented and applied in an acoustic velocity model using cross-correlational interferometry, although it could just as easily be applied with interferometry by deconvolution. The method uses an acquisition geometry consisting of an array of sources and receivers

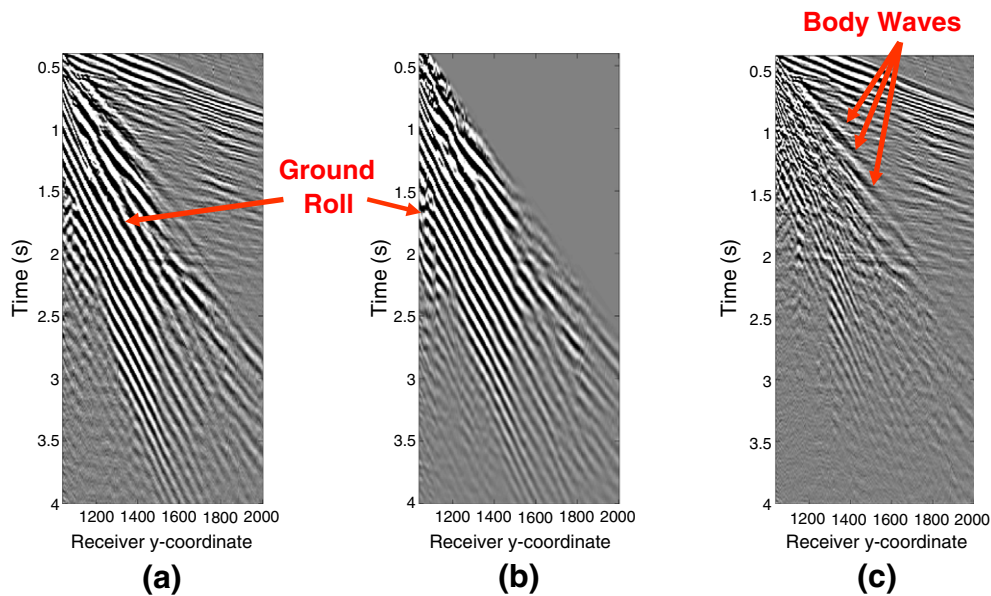


Fig. 16. Example of scattered ground-roll removal through seismic interferometry. (a) Raw data. (b) Ground-roll predicted from seismic interferometry. (c) Data obtained by subtracting the adaptively filtered ground-roll obtained through seismic interferometry from the raw data. Modified after Halliday (2010).

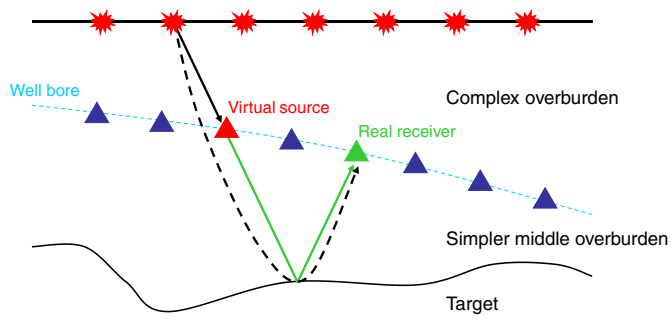


Fig. 17. Geometry of the so-called virtual source method of Bakulin and Calvert (2006). Receivers are located in the borehole, and record both the down-going wavefield through the complex overburden and the up-going reflected wavefield. By cross-correlating the waveforms recorded at two receivers, one receiver (red triangle) is turned into a virtual source, whose signal (green line) is recorded at the other receiver (green triangle).

such as that shown in Fig. 18(a) for a marine setting. Cross-correlations are computed for each source position using the approximate acoustic interferometric integral equation of Wapenaar and Fokkema (2006) (Eq. (16)), and the resulting traces are sorted into a correlation gather (like that in Fig. 9(b)). When each Green's function in the integral is considered as the sum of a direct and reflected component, a sum of four terms is obtained from Eq. (16), similarly to the case described by Snieder et al. (2006). Among these four terms, interferometric velocity analysis makes use of term T4, which is obtained from the cross-correlation of multiply-reflected waves, having the same (Fig. 18(b)) or different (Fig. 18(c)) numbers of bounce points from the reflector, at both receivers. King et al. (2011) call energy located to the left of the stationary points indicated by the green arrows in Fig. 18(c) *non-physical (np) energy*, since from an interferometric point of view it contains no stationary points and hence does not contribute to the physical energy that would propagate from one receiver location to the other. They use this

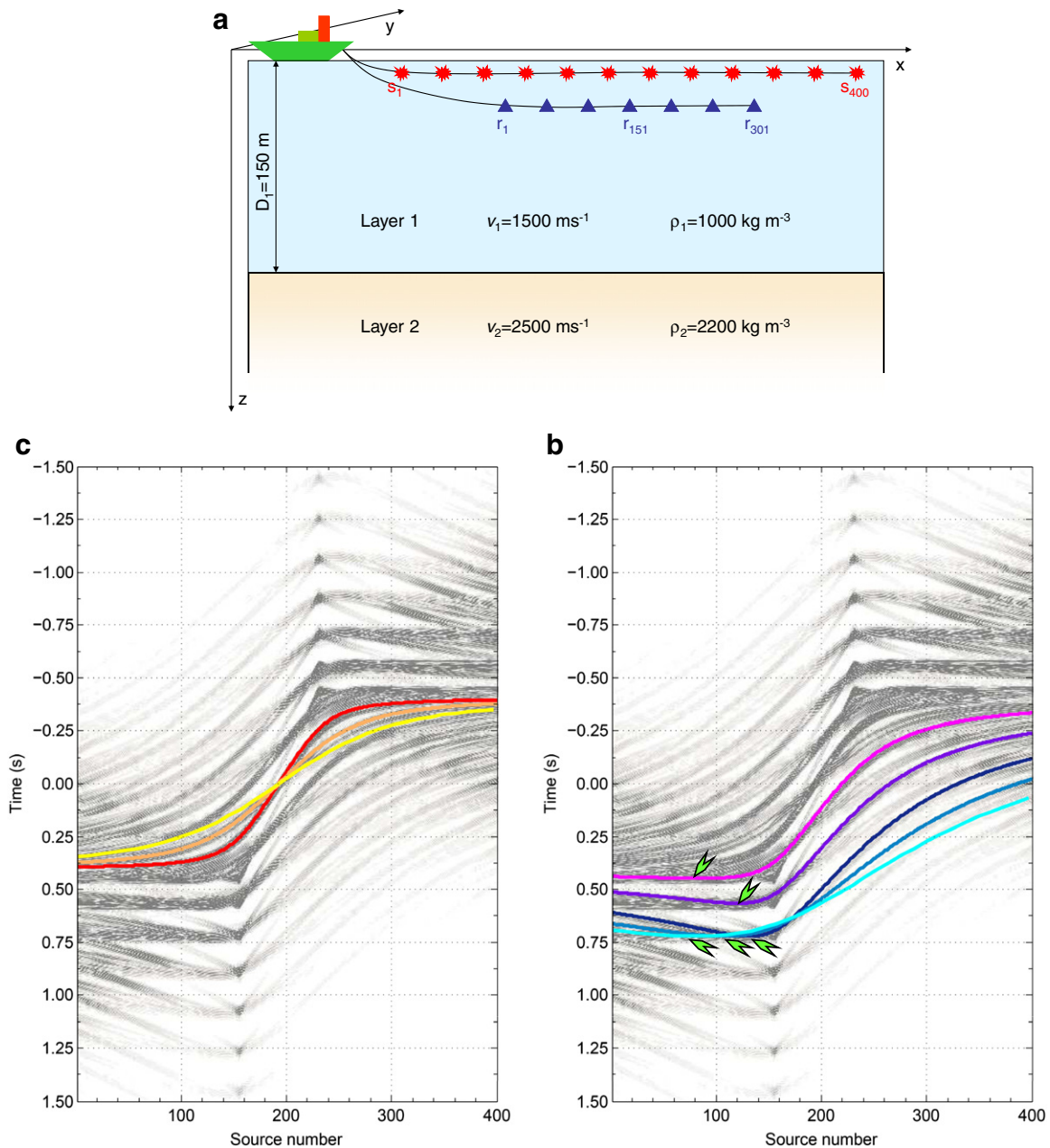


Fig. 18. (a) Schematic illustration of the 1-layer model used by King et al. (2011) for interferometric velocity analysis. Correlation gathers between receiver 1 and receiver 151 and travelttime curves of reflected waves having (b) the same and (c) a different number of bounce points. Plots courtesy of Simon King.

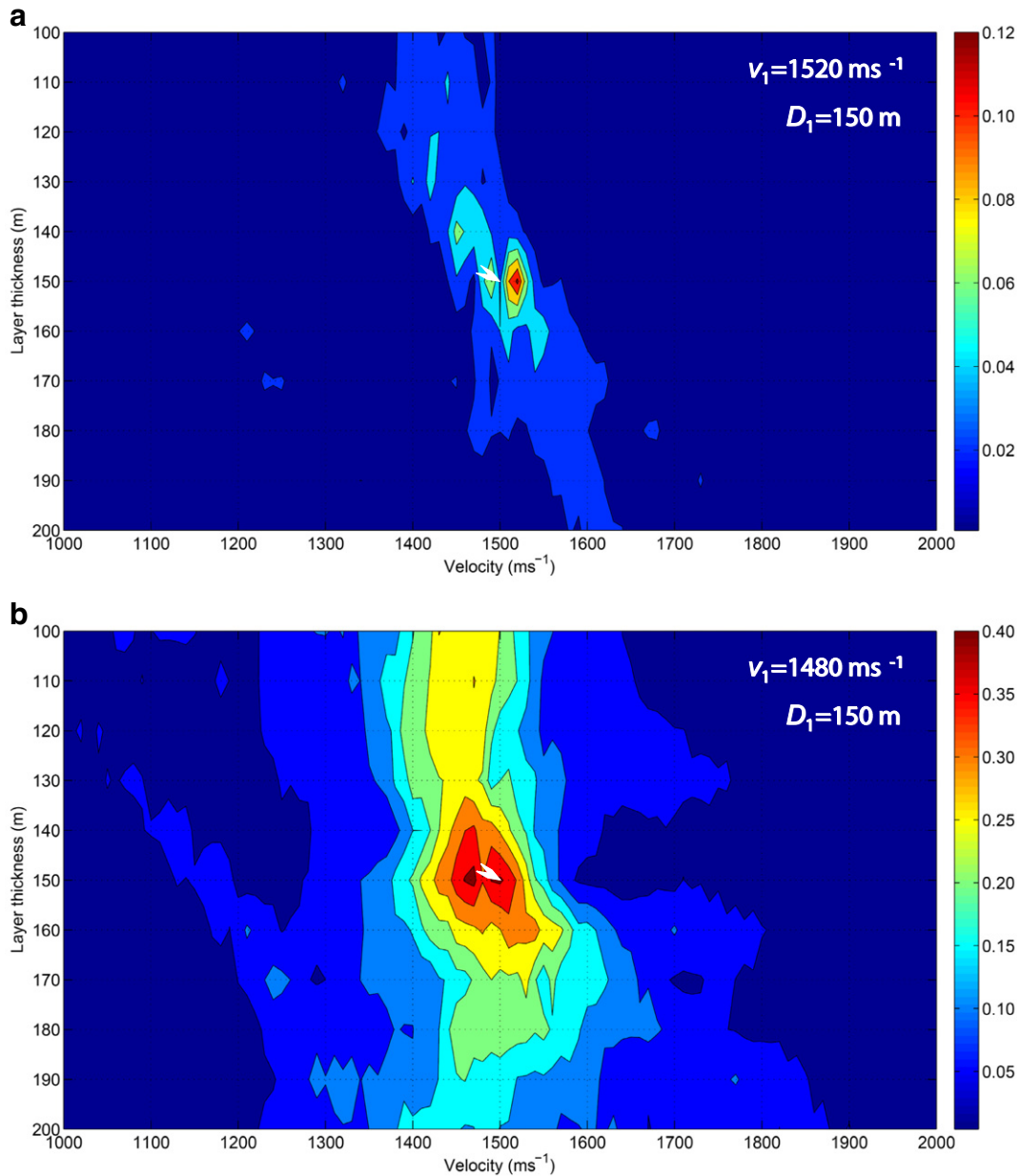


Fig. 19. Velocity-layer thickness spectra computed up to the 3rd order multiple for the 1-layer model shown in Fig. 18(a), using (a) all 400 sources, and (b) only the first 80 sources. The values of semblance are given by the colour scales on the right of the plots; white pointers indicate the true layer thickness and velocity, while the root-mean-square velocity and layer thickness values with higher coherency are indicated in the top-right corner. Plots courtesy of Simon King.

non-physical energy to constrain layer thickness and root-mean-square (rms) velocity.

In the 1-layer case, traveltime difference curves between waves recorded at two receivers (receiver 1 and receiver 151) are calculated for different layer depths (D_1), velocities (v_1) and number of bounce points at the interface. The coherency between the calculated traveltime difference curves and the curves in the correlation gather is assessed using the semblance measure (Neidell and Taner, 1971). Fig. 19 shows velocity-layer thickness spectra computed up to the 3rd order multiple using (a) all 400 sources, and (b) only the first 80 sources which are all located at far offsets from both receivers. Both spectra provide a layer thickness and velocity value which is close to the actual value (shown by the arrow). However, King et al. (2011) show that the maximum coherency value for 80 sources is three times larger than that for 400 sources, and suggest how better velocity and layer thickness estimates can therefore be

obtained by using fewer sources that provide only non-physical arrivals.

King et al. (2011) then repeat the same procedure for a multi-layer model. In this case, they suggest computing and subtracting terms T_1 , T_2 and T_3 from the correlation gather, in order to be left purely with term T_4 . A “layer-stripping” approach is then used in order to obtain estimates of the rms velocity and thickness of each layer. With this technique, rms velocity and thickness are obtained first for the top layer, by using the same method as for the 1-layer case, and then progressively for each deeper layer in turn, by using the results obtained for the layers above to “strip-off” their effects. Hence, compared to traditional velocity analysis, which may wrongly treat multiples as primaries, interferometric velocity analysis presents several advantages: multiples are correctly handled and used constructively in order to retrieve information on the subsurface, rather than being removed from the data; in addition, since only

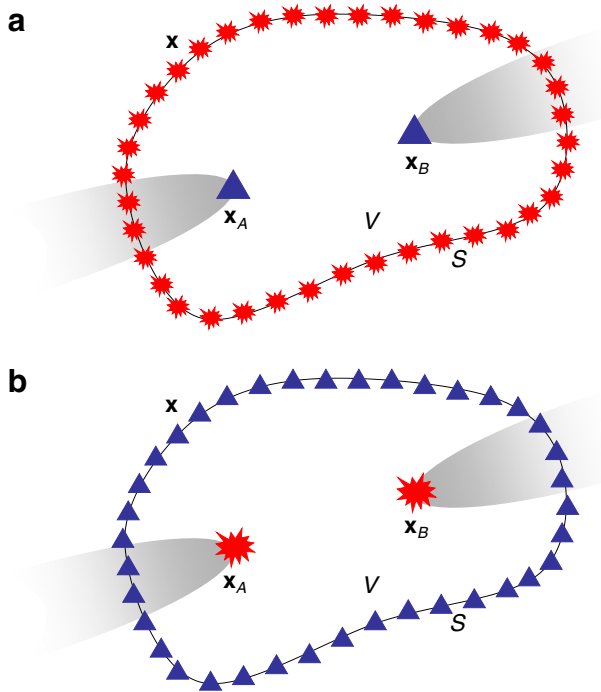


Fig. 20. Schematic geometries for seismic interferometry. (a) Inter-receiver interferometry by cross-correlation requires receivers to be placed within a boundary of sources. (b) Inter-source interferometry by cross-correlation requires sources to be placed within a boundary of receivers. In both cases, the stationary-phase approach shows that the Green's function can be approximated by only considering boundary sources (receivers) located along the extension of the line connecting the receivers (sources) – within the shaded areas.

two receivers can be considered at a time, the procedure can be repeated for many receiver pairs, providing a large number of estimates of layer thickness and velocity. However, as in all layer-stripping methods, errors during the initial stages may propagate and expand throughout the process, and prior geological knowledge is required in order to constrain the initial velocity and layer thickness values to a plausible range. In addition, the method is not applicable in the case of dipping layers. The important conclusion of this work is therefore that in some situations so-called non-physical energy may contain more information about the subsurface than physical energy.

7. Inter-source interferometry

The theory of inter-source interferometry arises directly from that of inter-receiver interferometry, by applying source-receiver reciprocity (Eq. (13)) to the interferometric integrals in Section 5.2 (Curtis et al., 2009). The starting points in the derivation are the source-receiver geometries shown in Fig. 20 and the interferometric integral by van Manen et al. (2005, 2006), for either the acoustic (Eq. (14)) or the elastodynamic (Eq. (17)) case.

Consider the geometry shown in Fig. 20(a): two receivers, located at \mathbf{x}_A and \mathbf{x}_B , are surrounded by a boundary of sources \mathbf{x} on S , and the shaded areas highlight those sources contributing constructively to the interferometric integral, as demonstrated by Snieder (2004). According to source-receiver reciprocity, the acoustic signal recorded at \mathbf{x}_A (\mathbf{x}_B) for a source at \mathbf{x} is equal to the signal recorded at \mathbf{x} for a source at \mathbf{x}_A (\mathbf{x}_B): $G(\mathbf{x}_A, \mathbf{x}) = G(\mathbf{x}, \mathbf{x}_A)$ and $G(\mathbf{x}_B, \mathbf{x}) = G(\mathbf{x}, \mathbf{x}_B)$ – Eq. (13). It is therefore possible to interchange sources and receivers and still record the same data. Interchanging sources and receivers results in the geometry in Fig. 20(b): two sources located at \mathbf{x}_A

and \mathbf{x}_B are surrounded by a boundary of receivers \mathbf{x} on S . Applying source-receiver reciprocity to the interferometric integral equations, the following expressions are obtained in the frequency domain:

$$\begin{aligned} \tilde{G}^*(\mathbf{x}_B, \mathbf{x}_A) - \tilde{G}(\mathbf{x}_B, \mathbf{x}_A) \\ = \int_S \frac{1}{\rho} \left[\left(\partial_j \tilde{G}(\mathbf{x}, \mathbf{x}_B) \right) \tilde{G}^*(\mathbf{x}, \mathbf{x}_A) - \tilde{G}(\mathbf{x}, \mathbf{x}_B) \left(\partial_j \tilde{G}^*(\mathbf{x}, \mathbf{x}_A) \right) \right] n_j dS \end{aligned} \quad (25)$$

in the acoustic case, and

$$\begin{aligned} \tilde{G}_{im}^*(\mathbf{x}_B, \mathbf{x}_A) - \tilde{G}_{im}(\mathbf{x}_B, \mathbf{x}_A) \\ = - \int_S c_{ijkl} \left[\left(\partial_k \tilde{G}_{li}(\mathbf{x}, \mathbf{x}_B) \right) \tilde{G}_{mn}^*(\mathbf{x}, \mathbf{x}_A) - \tilde{G}_{ni}(\mathbf{x}, \mathbf{x}_B) \left(\partial_k \tilde{G}_{im}^*(\mathbf{x}, \mathbf{x}_A) \right) \right] n_j dS \end{aligned} \quad (26)$$

in the elastodynamic case (Curtis et al., 2009), where ∂ acts on the receiver coordinate \mathbf{x} . In both cases, the reconstructed Green's function corresponds to the signal that would be recorded at \mathbf{x}_B , due to a source at \mathbf{x}_A , if a receiver, rather than a source, were placed at \mathbf{x}_B . Hence, in contrast to inter-receiver interferometry, these two equations allow the Green's function between two sources, \mathbf{x}_A and \mathbf{x}_B , to be obtained from wavefields recorded on a surrounding boundary of receivers S , by turning one of the sources into a virtual receiver. In addition, by using the stationary-phase approach as earlier, it can be shown that receivers need not necessarily be placed all along boundary S , but only near the extension of the ray path connecting the sources (shaded area in panel (b)).

Just as inter-receiver interferometry obviates the need for seismic sources in aseismic areas, inter-source interferometry between two earthquake sources allows virtual receivers to be created within seismic areas that may not be well covered by receiver networks (e.g. Central Africa, the Tibetan and Andean Plateaux). What is more, since earthquakes are by definition in the Earth's subsurface, so are the virtual receivers. Curtis et al. (2009) show that the resulting measured seismograms constructed in this way are actually records of the dynamic strain caused by passing waves from the other earthquake (rather than measures of displacement as obtained from normal seismometers). The components of strain measured are precisely those represented in the original earthquake source mechanisms: virtual sensors constructed from thrust or normal fault earthquakes measure the strain difference in the vertical and horizontal plane; those constructed from strike-slip earthquakes measure shear strain in the horizontal plane, and, finally, those constructed from explosions or implosions measure the volumetric expansion or contraction of the subsurface.

Curtis et al. (2009) apply the method of inter-receiver interferometry to data recorded at the USArray and Berkeley seismic networks in California (Fig. 21(a)): earthquakes 3 (strike-slip) and 4 (normal) are turned into virtual sensors and used to record other earthquakes occurring in the region; these virtual records are then compared to actual records obtained at recording stations located near the virtual sensors. In the case of earthquake 1, a comparison between the sum of the horizontal strain components (solid line), from the virtual sensor at 3, and the inverted time-derivative of the radial component of velocity from actual recordings (dashed line) is shown in the top image of Fig. 21(b): the difference between the surface wave arrival times is less than 5 s for both the main energy envelope and individual phase arrival times, the difference being explained by the difference in location and in temporal response between real and virtual seismometers. The middle image of Fig. 21(b) shows a comparison between the real vertical component of particle velocity for event 1 recorded near sensor 4 (dashed line) and the difference between strain components e_{33} and e_{11} from virtual receiver 4: as in the previous case, group arrival times match, while phases do not. However, if the same virtual recording is compared with real measurements of the e_{11} strain component (approximated by the measured, inverted

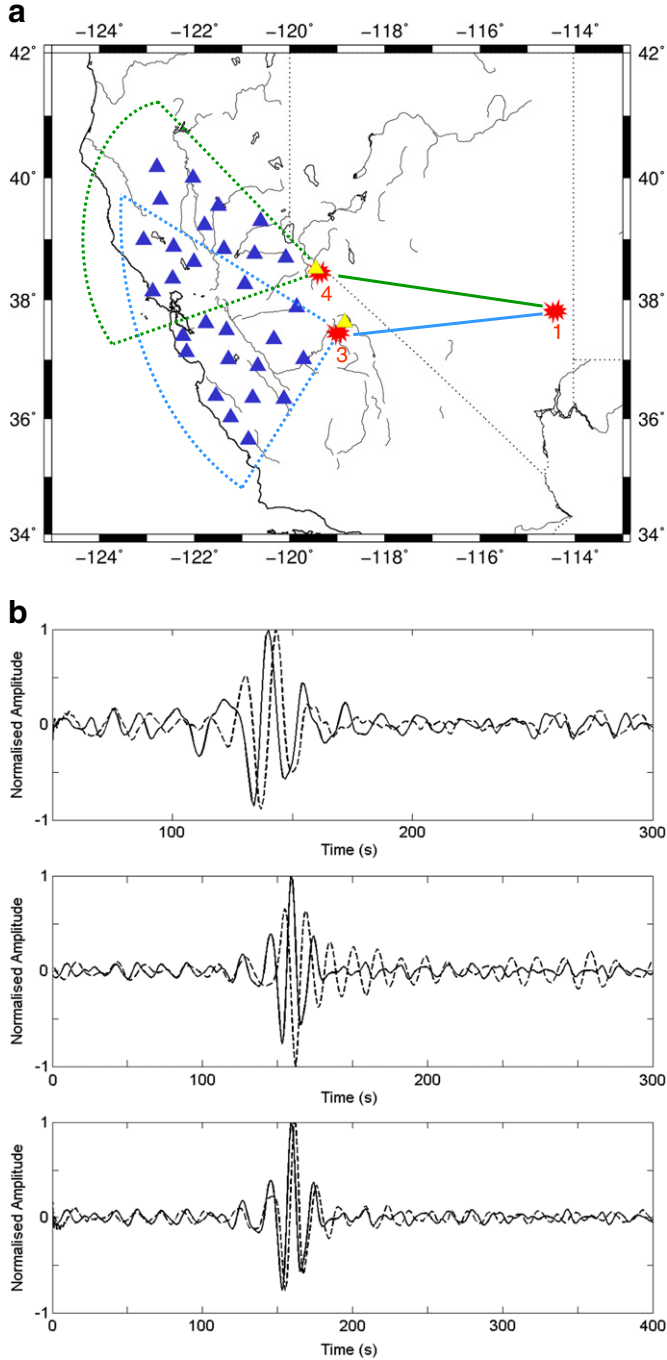


Fig. 21. (a) Earthquakes (red stars) and seismic stations (blue triangles) used for the application of inter-source interferometry in California. The virtual receivers are indicated by yellow triangles. (b) Comparison of virtual-receiver (solid lines) and real (dashed lines) seismic records: (top) earthquake 1 recorded at sensor 3, (middle) earthquake 1 recorded at sensor 4 (difference between vertical and horizontal strain components), (bottom) earthquake 1 recorded at sensor 4 (approximation to e_{11} component of strain). Map in (a) redrawn after Curtis et al. (2009) using the GMT (Generic Mapping Tools) package; seismograms in (b) courtesy of Heather Nicolson.

time-derivative of radial particle velocity measurements), an extremely good match is observed (Fig. 21(b), bottom image).

Hong and Menke (2006) previously used a related but different method that employs only the coda of the recorded seismograms from the earthquake pair. Similar to Campillo and Paul (2003) they appeal to the diffuse-wavefield (highly scattered) version of interferometric theory rather than to the exact representation theorems

given above. However, Curtis et al. (2009) show that by using only the coda all of the main, directly-propagating energy between the two source locations is removed, and since the requirement of a strongly scattering medium may not hold this leads to errors in the results (indeed, in a non-scattering medium such a method can not work at all). Hence, using all of the recorded energy including the direct waves, and appealing to the representation theorem approach above appears to be advantageous.

Tonegawa and Nishida (2010) show that the method of Curtis et al. (2009) can also be applied to obtain inter-earthquake body waves. Using pairs of events within a subducting slab recorded on a neighbouring dense network of seismometers across Japan, they are able to obtain approximate Green's functions and time-versus-distance relationships for body wave propagation within the slab. This is the first time that recordings have been made on (virtual) seismometers within the subducting lithosphere, and one of the first publications to successfully extract body wave information from interferometric correlations at a regional scale.

Besides its applications in earthquake seismology where it can be used to monitor dynamic strain caused by passing seismic waves, the method of inter-source interferometry is also useful in exploration seismology. For example, active sources in a seismic survey can be turned into virtual sensors, producing many more measurement locations (Halliday et al., 2010a). Also, the fact that virtual seismometers can also provide non-invasive measurements within the interior of the Earth means that they may be able to be created directly within resource reservoirs in the subsurface without drilling.

8. Source-receiver interferometry

The method of source-receiver interferometry, arises from a combination of inter-receiver and inter-source interferometry (Curtis and Halliday, 2010b). It allows the wavefield between an actual source and an actual receiver to be reconstructed from only recordings obtained from surrounding boundaries of receivers and sources (i.e. without using the measured source-to-receiver wavefield). In so doing, the real source and the real receiver are converted into a virtual receiver and a virtual source, respectively. While this may not seem to be particularly useful from a practical point of view, we show below that it has several important ramifications.

So far in the geophysical literature, source-receiver interferometric integrals have been derived for the three configurations shown in Fig. 22, in both the acoustic and elastic case (Curtis and Halliday, 2010a). The derivations for source-receiver interferometry involve creating a unified representation theorem, obtained from the reciprocity theorems of the convolution and correlation type. In the acoustic case, the following expression is obtained in the frequency domain for the configuration shown in Fig. 22(a):

$$\begin{aligned} & \widehat{G}^*(\mathbf{x}_B, \mathbf{x}_A) + \widehat{G}(\mathbf{x}_B, \mathbf{x}_A) \\ &= \frac{1}{\omega \rho} \int_S \left\{ \left[\frac{-1}{\omega \rho} \int_S \left\{ \widehat{G}(\mathbf{x}', \mathbf{x}_A) (\partial_j \widehat{G}^*(\mathbf{x}', \mathbf{x})) - (\partial_j \widehat{G}(\mathbf{x}', \mathbf{x}_A)) \widehat{G}^*(\mathbf{x}', \mathbf{x}) \right\} n_j dS' \right] (\partial_j \widehat{G}(\mathbf{x}_B, \mathbf{x})) \right. \\ & \quad \left. - \left(\partial_j \left[\frac{-1}{\omega \rho} \int_S \left\{ \widehat{G}(\mathbf{x}', \mathbf{x}_A) (\partial_j \widehat{G}^*(\mathbf{x}', \mathbf{x})) - (\partial_j \widehat{G}(\mathbf{x}', \mathbf{x}_A)) \widehat{G}^*(\mathbf{x}', \mathbf{x}) \right\} n_j dS' \right] \right) \widehat{G}(\mathbf{x}_B, \mathbf{x}) \right\} n_j dS, \end{aligned} \quad (27)$$

where $\widehat{G}(\mathbf{x}_B, \mathbf{x}_A)$ represents the pressure Green's function between an impulsive source at \mathbf{x}_A and a receiver at \mathbf{x}_B . Similar expressions can be found in Curtis and Halliday (2010a) for the source-receiver geometries represented in Fig. 22(b) and (c).

Although this expression may look complicated, its meaning can be explained by examining it in conjunction with the corresponding source-receiver geometry. The terms in square brackets use the boundary of receivers just as in Eq. (25) to turn the source at \mathbf{x}_A into a virtual receiver that records each of the boundary sources \mathbf{x}

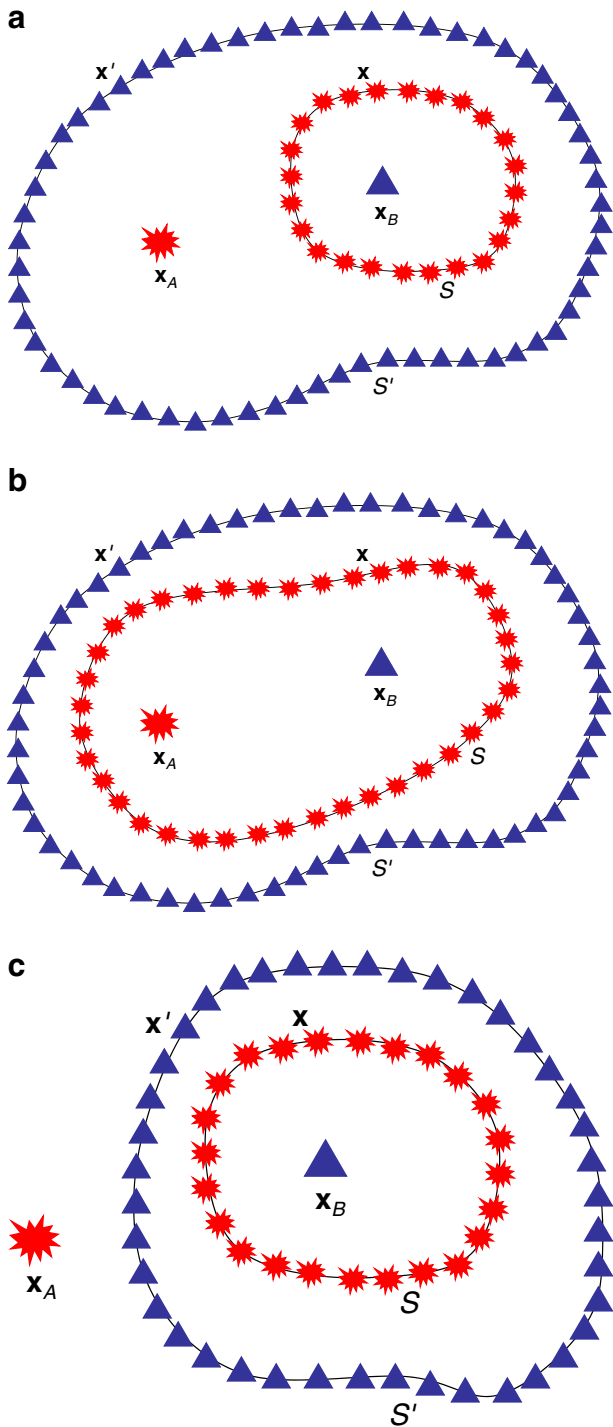


Fig. 22. Schematic canonical geometries for source-receiver interferometry for which interferometric formulae are given in Curtis and Halliday (2010a). Receivers are represented by blue triangles and sources are represented by red explosions.

in turn. Cross-correlation is used for the configurations in panels (a) and (b) as the boundary of receivers surrounds all sources, while convolution is used for the configuration in panel (c) as the boundary of receivers does not surround source \mathbf{x}_A . Then, in the outer integral, this new virtual receiver is used to construct the Green's function between \mathbf{x}_A and \mathbf{x}_B by using the boundary of sources \mathbf{x} on S , turning \mathbf{x}_B into a virtual receiver, this latter step using equations like Eq. (24), for the geometries in panels (a) and (c), and like Eq. (15) for the geometry in panel (b).

However, dipolar sources (represented by the derivatives of the Green's functions) and closed boundaries of sources and receivers may not always be available in practical applications. Hence, in order to apply these formulae, some approximations may be needed. These approximations may include expressing dipolar sources in terms of monopolar sources ($\mp ikG = n_j \partial_j G$) assuming Sommerfield conditions hold (Born and Wolf, 1999), and considering only boundary sources and receivers that are located near the line connecting \mathbf{x}_A and \mathbf{x}_B , as stationary-phase analysis shows that these are the ones that provide constructive contributions to the interferometric integral. The resulting simplified equation for the geometry in Fig. 22(a) is

$$\widehat{G}^*(\mathbf{x}_B, \mathbf{x}_A) + \widehat{G}(\mathbf{x}_B, \mathbf{x}_A) \approx \frac{4k^2}{(\omega\rho)^2} \int_S \int_{S'} \widehat{G}(\mathbf{x}', \mathbf{x}_A) \widehat{G}^*(\mathbf{x}', \mathbf{x}) \widehat{G}(\mathbf{x}_B, \mathbf{x}) dS' dS \quad (28)$$

(Curtis, 2009; Curtis and Halliday, 2010a). The method was demonstrated to work well in practice on a test industrial seismic data set by Duguid et al. (2011); indeed, in that application source-receiver interferometry gave improved results compared to inter-receiver or inter-source interferometry.

This new type of interferometry presents several advantages and potential applications compared to the previous two forms, and just as the equations in Curtis and Halliday (2010a) were derived by combining convolutional and cross-correlational interferometry for the geometries shown in Fig. 22, similar equations can be derived for many different source-receiver geometries, for deconvolutional interferometry in place of correlational interferometry, and even combining passive and active sources (Curtis and Halliday, 2010a). Examples of possible applications in exploration seismology include the creation of synthetic source-receiver records which were not directly recorded, for instance for the removal of ground-roll from reflection data sets. This application may be useful in cases where the direct recording between \mathbf{x}_A and \mathbf{x}_B is not available, while recordings between \mathbf{x}_A and many other receivers are. For interferometric ground-roll removal, source-receiver interferometry would provide similar surface wave estimates to the inter-receiver method used by Halliday et al. (2007, 2010a), but with the advantage that receivers would not be required beside each shot location, perhaps making this design more economically viable: Duguid et al. (2011) perform ground roll removal on a seismic data set to reveal underlying scattered arrivals that were otherwise hidden by the directly-propagating surface waves. Also, if real records between \mathbf{x}_A and \mathbf{x}_B were also available, source-receiver interferometry could be used to assess the limitations of seismic interferometry given practical conditions, by comparing the real and virtual records obtained between \mathbf{x}_A and \mathbf{x}_B .

In other applications, Poliannikov (2011) shows that, using only receivers in a subsurface well and sources on the surface similarly to Fig. 17, inter-receiver interferometry usually only provides top-side reflections for reflectors below the well, whereas a particular application of source-receiver interferometry also provides underside reflections from reflectors above the well. Additionally, King and Curtis (2012) show that the second integration in source-receiver interferometry actually corrects errors (the existence of non-physical energy) made in the first integration (which is equivalent to an application of standard inter-receiver interferometry).

However, perhaps the most fundamental result of source-receiver interferometry theory to-date is that Halliday and Curtis (2010) show that it is directly and analytically related to the imaging theory of Oristaglio (1989), a theorem that describes how many modern imaging algorithms work. This link had been postulated by authors previously (Thorbecke and Wapenaar, 2007; Wapenaar, 2007; Vasconcelos, 2008), but could not be derived analytically because either only a single boundary of sources (Fig. 20(a)) or receivers (Fig. 20(b)) were considered in inter-receiver or inter-source

interferometry, respectively. Imaging theory always uses both sources and receivers, hence source-receiver interferometry is the first interferometric form that could be related directly to prove the link. Vasconcelos et al. (2010) use this or similar theory to perform localised velocity analysis in the subsurface using what they call “extended images”, and Halliday and Curtis (2010) show precisely how source-receiver interferometry can be thought of as a new, non-linear imaging method. What is more, Halliday et al. (2010b) extend the theory of source-receiver interferometry to body waves, retrieving dynamically-correct interferometric expressions for both reflected and converted P- and S-wave responses between sources and receivers. In doing so, Halliday et al. (2010b) derive a generalised form of the $PP + PS = SS$ equation (Grechka and Tsvankin, 2002; Grechka and Dewangan, 2003), which describes the relationship between PP (i.e. reflected P-wave), PS (i.e. S-wave generating from the reflection and conversion of a P-wave) and SS (i.e. reflected S-wave) waves. These new expressions may find application in acquisition and processing, imaging and inversion of seismic data, allowing a dynamically-correct estimate of SS waves to be made from PP and PS responses alone.

9. Time-dependent monitoring and green's functions from late seismic codas

Coda wave interferometry (CWI) is a technique for subsurface monitoring which makes use of recordings of multiply scattered waves in order to infer time-dependent changes within the medium. While the directly arriving phases only sample the medium along the (perhaps virtual) source-receiver path (Fig. 23(a)), coda waves have a much longer propagation path due to multiple scattering (Fig. 23(b)) and are therefore sensitive to changes within a much larger volume of the medium. Consequently, if a perturbation in the medium (i.e. a bulk variation in velocity, scatterer positions, etc.) occurs over time, it can often be identified by a change in travel-time of the coda waves when this change is undetectable in the first arrivals (Snieder et al., 2002; Snieder and Hagerty, 2004; Grêt et al., 2005; 2006a; 2006b; Pandolfi et al., 2006; Nagaoka et al., 2010; Zhou et al., 2010).

An example of this application is illustrated in Fig. 24, which shows the responses recorded on the Merapi volcano in Java due to an impulse fired by an air gun, as in the study presented by Snieder (2003). The two waveforms, recorded a year apart in time, appear to match when the early arrivals are considered (Fig. 24(b)). In contrast, the late coda waveforms (Fig. 24(c)) do not match and appear

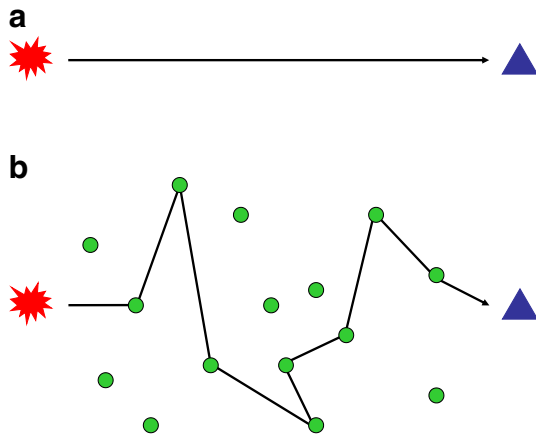


Fig. 23. Comparison of direct and scattered coda wave raypaths from a source (red explosion) to a receiver (blue triangle). (a) A direct wave follows the shortest path between the source and the receiver. (b) A coda wave travels a longer path due to scattering off heterogeneities (green circles).

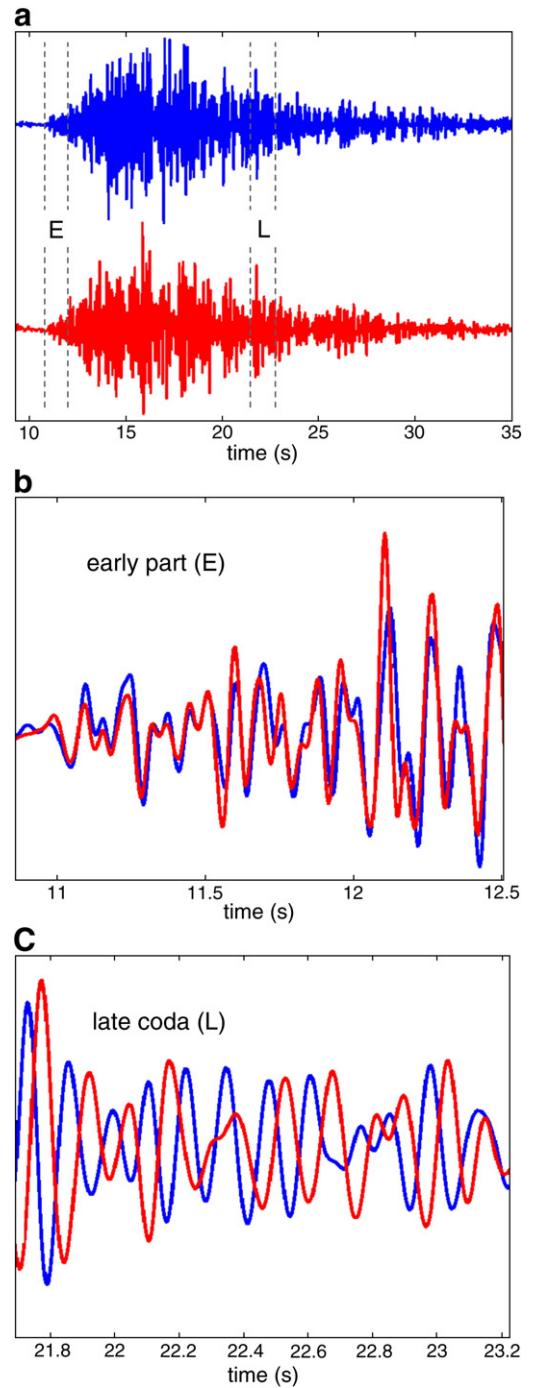


Fig. 24. Comparison of waveforms recorded at Merapi volcano for the same source and receiver a year apart in time: (a) complete waveforms; (b) early arrivals; (c) late coda. Seismograms courtesy of Roel Snieder.

to be shifted in time, as a result of changes that occurred within the interior of the volcano.

The differences in the waveforms recorded before and after the perturbation can be quantified using the normalized cross-correlation coefficient $R(t_s)$ defined by Snieder et al. (2002). The unperturbed wavefield $u^{(u)}(t)$ (i.e., the wavefield before perturbation of the medium) and the perturbed wavefield $u^{(p)}(t)$ (that recorded after perturbation of the medium) can be respectively denoted by

$$u^{(u)}(t) = \sum_T A_T(t) \quad (29a)$$

and

$$u^{(p)}(t) = \sum_T A_T(t - \tau_T), \quad (29b)$$

where $A_T(t)$ is the wave propagating along scattering trajectory T and the summation signs denote the sum of all waves scattered along all possible paths, t is time and τ_T is the time shift between waveforms propagating along trajectory T before and after the perturbation. The correlation coefficient between the coda of the unperturbed and perturbed wavefields can be defined as

$$R(t_S) \equiv \frac{\int_{t-t_w}^{t+t_w} (u^{(u)}(t')) (u^{(p)}(t' + t_S)) dt'}{\left(\int_{t-t_w}^{t+t_w} (u^{(u)}(t'))^2 dt' \int_{t-t_w}^{t+t_w} (u^{(p)}(t'))^2 dt' \right)^{1/2}}, \quad (30)$$

where the correlation time-window of width $2t_w$ is centred at time t , and t_S is the correlation time-shift between the unperturbed and perturbed waveforms. The correlation coefficient $R(t_S)$ attains its maximum value $R(t_{\max})$ when the correlation time-shift t_S is equal to the average time-shift $\langle \tau \rangle$ of the waveforms in the correlation time-window considered:

$$t_{\max} = t_S = \langle \tau \rangle. \quad (31)$$

This maximum correlation value $R(t_{\max})$ is related to the variance of the traveltimes perturbation σ_τ^2 according to

$$R(t_{\max}) = 1 - \frac{1}{2} \bar{\omega}^2 \sigma_\tau^2, \quad (32)$$

where $\bar{\omega}^2$ is the mean-squared angular frequency of the waves arriving in the time window (Snieder et al., 2002). Hence, from the cross-correlation of coda waves, it is possible to calculate both the mean and the variance of the time-shift before and after the perturbation using Eqs. (31) and (32).

Snieder et al. (2002) identify three types of perturbations that affect the coda: these include a change in the velocity of the medium, a variation in scatterers' locations, and the displacement of the source position. Each of these perturbation types influences the scattered wavefields in a different way and has a distinct effect on the coda: velocity perturbations can be identified by a linearly increasing magnitude of shift in t_{\max} ; changes in scatterers' positions instead cause the maximum cross-correlation value $R(t_{\max})$ to decrease with time; finally, a variation in source location only affects the path between the source and the first scatterer, and the maximum cross-correlation value $R(t_{\max})$ is independent of time.

For a constant velocity perturbation δv and fixed scatterer and source locations, the relative velocity change $\delta v/v$ can be obtained from the ratio of the time-shift $\langle \tau \rangle$, which gives the maximum cross-correlation coefficient, and the centre time t :

$$\frac{\delta v}{v} = - \frac{\langle \tau \rangle}{t}. \quad (33)$$

If the velocity of the medium does not vary with time but a change in scatterer location occurs, the root mean square of the scatterer displacement can be calculated provided the wave velocity v and the transport mean free path l^* (Maret, 1995; Legendijk and van Tiggelen, 1996) are known:

$$\delta^2 = (1 - R(t_{\max})) \frac{v l^*}{\bar{\omega}^2 t}. \quad (34)$$

Finally, if the variations in the coda occur as a result of a change in position of the source, the source displacement distance δ can be calculated from

$$\delta^2 = \left(2v^2 / \bar{\omega}^2 \right) (1 - R(t_{\max})). \quad (35)$$

Snieder et al. (2002) demonstrated the applicability of the theory of coda wave interferometry by conducting laboratory experiments on a granite sample. The waveforms obtained at different temperatures show a decorrelation of the scattered coda with increasing temperature, which corresponds to a structural change (thermal expansion and potentially cracking) occurring within the sample as the temperature increases.

Grêt et al. (2005) applied coda wave interferometry to seismic records from a number of Strombolian eruptions at Mount Erebus volcano, Antarctica. Their results showed a decreasing correlation of codas following different events as a result of changes in the scattering properties of the volcanic edifice due to an evolution of its structure. What is more, these changes could not be detected by early (more direct) arrivals, proving how the sensitivity of coda waves to structural variations within the medium exceeds that of direct waves.

Brenguier et al. (2008b) successfully combined the methods of seismic interferometry presented in the preceding sections with coda wave interferometry described here, to create a powerful new monitoring methodology. They applied time-dependent monitoring techniques of coda wave interferometry to seismic records obtained from virtual sources constructed between receiver pairs at Piton de la Fournaise volcano, La Réunion Island. By using inter-receiver interferometry, they constructed reference Green's functions between all possible pairs of receivers in the network using 18 months of passive noise data. Green's functions along identical paths were then repeatedly computed by cross-correlating seismic noise records from only ten-day-long windows. By moving the windows forward in time through the 18 month period and comparing the windowed Green's function estimates with the reference Green's functions, Brenguier et al. (2008b) succeeded in identifying temporal changes in seismic velocities within the volcanic edifice that resulted from structural changes in the subsurface. In particular, seismic velocities were found to decrease (up to -0.05%) before volcanic eruptions, as a result of dilatation of the edifice due to the increased pressure in the magma.

Using a similar technique based on the cross-correlation of ambient noise records, Brenguier et al. (2008a) were able to detect reductions in seismic velocity around the San Andreas fault zone before the 2003 San Simeon and the 2004 Parkfield earthquakes. The velocity perturbations were found to relax over time to initial levels and to agree with the relaxation curve of along-fault displacement obtained from GPS measurements. From these observations, Brenguier et al. (2008a) suggest that co-seismic velocity changes are related to co-seismic damage in the shallow layers and stress changes at depth, and also to post-seismic stress relaxation. Again, velocity changes of -0.04% to -0.08% were observed robustly, showing the accuracy of this new method.

What is particularly interesting about the above two applications is that the Green's function estimates used for monitoring were fairly poor due to the short time period of noise employed for their construction (10-day intervals in Brenguier et al., 2008b). Nevertheless, the phase of the signal in the erroneous Green's functions appears stable enough to obtain robust readings of phase changes over time. Since the errors in the Green's functions may be thought of as non-physical arrivals due to an incomplete boundary of noise sources firing within each of the short time periods considered, this again attests to the fact that non-physical energy contains a great deal of useful information, provided we can work out how to extract it.

Similar studies that applied the method of Passive Image Interferometry to monitor seismic velocity changes in the subsurface were also conducted by Sens-Schönfelder and Wegler (2006), Wegler and Sens-Schönfelder (2007), Ohmi et al. (2008) and Wegler et al. (2009). Similarly, Kraeva et al. (2009) studied changes in Green's functions obtained from cross-correlation of noise recordings, and attributed the seasonal variation pattern to microseismic activity induced by ocean storms in the deep ocean.

10. Discussion

While traditional seismology regards background noise as a perturbation to desired recordings of earthquake waves, seismic interferometry allows the retrieval of useful information from ambient seismic waves propagating between two receiver locations without the need for an identifiable active source of energy. The main theoretical requirement for this to be robust across different media with only monopolar or only dipolar noise sources is that the sources are both far from, and completely surround one or both of the receivers in question. However, recent developments have shown how noise sources generally need to be located only along the extension of the ray path connecting the two receiver positions, provided that the medium is not too strongly scattering off this ray path (Snieder, 2004; Snieder et al., 2006).

When noise is poorly distributed or arrives with a significantly biased amplitude from different directions, a number of techniques have been developed to compensate to varying extents for this biased directionality (Curtis and Halliday, 2010b; Douma and Snieder, 2006; Mehta et al., 2007; van der Neut and Bakulin, 2008; Wapenaar and van der Neut, 2010; Wapenaar et al., 2008; 2011). The introduction of seismic interferometry by cross-convolution has also allowed the method to account for attenuation and to be safely applied to media with losses, hence providing more accurate and realistic Green's function reconstructions (Slob et al., 2007; Halliday and Curtis, 2009b).

What is important for tectonophysical applications is that local earthquakes are no longer needed to image the crust and mantle locally. Imaging is now possible between seismic stations, in addition to below individual seismometers as was already possible using conventional receiver functions analysis. Interferometry provides a means to construct seismograms as though local sources of energy existed at receiver locations; hence, it is important that seismometers are moved in networks (not only as individual instruments) to those huge areas of the Earth over which we currently have relatively sparse information about the subsurface due to the low density of both stations and earthquakes (e.g., Africa, Siberia, ocean floors, etc. – Fig. 4).

By interchanging sources and receivers, it was shown how seismic interferometry could be used to create virtual seismometers out of earthquakes themselves; since earthquakes are by definition within the Earth's subsurface, so are the virtual seismometers (Hong and Menke, 2006; Curtis et al., 2009). Both Curtis et al. (2009) and Tonegawa and Nishida (2010) have shown that this allows virtual recordings of seismic waves to be made within subducting lithospheric slabs, and Tonegawa and Nishida (2010) used these to estimate body wave velocities within or around the slab. Such localised recordings in the deep subsurface have not previously been possible to observe, and it is likely that future applications of the method will lead to significantly more detailed information about slab and mantle structure and properties. In addition, the ability to use earthquakes as sensors in relatively remote areas such as the Tibetan or Andean plateaux or mid-oceanic ridges where it is difficult to place real sensors may allow more detailed information about those areas to be obtained in future. In Tibet, for example, related techniques of inter-source surface wave phase velocity analysis have already been used (Romanowicz, 1982; Brandon and Romanowicz, 1986; Curtis and Woodhouse, 1997); interferometric analysis could extend such

methods from only kinematic (travel time) information to dynamic information.

Curtis et al. (2009) showed that virtual seismometers constructed from earthquake sources measure components of dynamic strain, rather than displacement as measured by real seismometers. Recent work has shown the potential for large magnitude, remote seismic events that send powerful dynamic wavefields through an area, to change the seismogenic strength of the crust in that area (Taira et al., 2009). The change in strength is shown to be manifest as a higher propensity to earthquake failure. The ability to measure dynamic strain components of passing seismic waves within the subsurface using seismic interferometry is therefore potentially of significant benefit, both to provide quantitative data about the mechanisms of earthquake triggering implied above, and to aid prediction of future propensity to failure.

The ability to reconstruct unrecorded source-to-receiver records using only boundaries of other distant sources and receivers (Curtis and Halliday, 2010b) has several implications as yet unrealised. First, it is in principle possible to synthesise unrecorded seismograms between earthquakes and stations for stations that were not installed at the time of the earthquake. It is therefore possible to create such seismograms for stations installed after the earthquake occurred – for example, rapid-deployment arrays installed immediately after large events. While such arrays are used to locate aftershocks of large events, they are not currently able to be used to locate the main event. If seismograms for the main event can be synthesised for seismometers in these arrays, 'acausal' local event location and characterisation (acausal because the event preceded the array's existence in time) using such arrays may become a practical possibility.

Another implication of source-receiver interferometry was explored by Halliday and Curtis (2010) who showed that this form of interferometry is directly and analytically related to linearised imaging theorems (Oristaglio, 1989). They showed that a new, nonlinear imaging relationship is created directly from source-receiver interferometric theory. This relationship creates a new perspective on subsurface imaging that does not require that waves scatter only once from diffractors as most current imaging algorithms assume, and which is consistent with the Optical Theorem of Physics (see below). The challenge is to translate this relationship into a practical and stable algorithm to construct images. In fact, first steps have already been taken by Sava and Vasconcelos (2009) and Vasconcelos et al. (2009a, 2009b). They use theory closely related to source-receiver interferometry to perform local velocity analysis around a fixed set of points in a subsurface image. This closes part of the gap between standard velocity analysis or tomography, and imaging theory. Future work will develop new ways to capitalise on the new methods to perform imaging directly.

Coda wave interferometry is now used by many groups around the world to monitor changes in subsurface properties over time (Snieder and Hagerty, 2004; Grêt et al., 2005; 2006a; Pandolfi et al., 2006; Nagaoka et al., 2010; Zhou et al., 2010). This method has been shown to be up to two orders of magnitude more accurate than existing industrial time-lapse monitoring methods (e.g., seismic velocity changes detected by Brenguier et al. (2008a) appear to be robust to less than 0.005%). However, the high accuracy is achieved only for a bulk change in the average background velocity across a region, hence this method currently trades off spatial resolution in favour of increased accuracy of velocity estimates. A future challenge is to develop extensions to the existing methodology that allow this trade-off to be controlled explicitly or implicitly, such that we can choose the level of deterioration in spatial resolution that we are willing to tolerate for a certain increase in accuracy of velocity estimates.

However, what is clear from discussions with practitioners and collaborators around the world (and from the authors' own investigations) is that many CWI studies of seismic properties do not show clear temporal changes during active volcanic eruptions, and that

such negative results have not been widely published to-date. This 'bias-towards-positivity' creates the potential illusion that this method works well in most cases. It is important that negative results are also analysed and published in future, to clarify whether there is some underlying assumption of the method that is not fulfilled in each particular case, or whether there really is no temporal change in average velocity at the scale of the average seismic wavelengths observed.

There are other areas of Physics that have been extended profoundly by the development of interferometry. Snieder *et al.* (2008) showed that at a scatterer (diffractor) the cancellation of the T4 term when summed with T2 and T3 in Fig. 8 requires that the Generalised Optical Theorem of classical Physics be adhered to at the scatterer. The Generalised Optical Theorem describes how energy is distributed as a function of angle during the diffraction of a wave at the scatterer (Wapenaar *et al.*, 2010b), and Snieder *et al.* (2008) showed that if one writes out the required cancellation between terms T2, T3 and T4 explicitly as an equation, it can be rearranged to create a proof or a derivation of the optical theorem directly. While Snieder *et al.* (2008) used this method to re-derive the Generalised Optical Theorem for acoustic waves, Halliday and Curtis (2009a) showed that the same method could be used to derive completely new optical theorems. They thus derived the first such theorem for elastic surface waves, which is also the first to exist for inhomogeneous media (some surface waves only exist in inhomogeneous media). From the structure of such derivations it is also clear that some kind of 'super-generalised' optical theorem that is valid for multiple media and wave types must emerge as a result of this theory in the near future.

The implications for Earth science are important: currently subsurface migration or imaging methods usually employ the so-called Born approximation (which implies that the physics of scattering is linearised and that only single-scattering occurs – see Wapenaar *et al.*, 2010b). Since true scattering is nonlinear, the Born approximation results in incorrect amplitudes in the constructed images. Snieder *et al.* (2008) showed that interferometry is implicitly consistent with the Optical Theorem and hence with the true, nonlinear scattering processes inside the Earth, and since also Halliday and Curtis (2010) showed how interferometry can potentially be used to construct new, nonlinear imaging algorithms, such imaging algorithms can also be consistent with the true scattering mechanisms in subsurface diffractors. Thus, as a result of future developments Earth images should become more consistent with physical reality.

Since its origin, the field of seismic interferometry has shown great promise in many areas of seismology. In addition, because its principles are not restricted to seismic waves but can also be applied to electromagnetic, acoustic, seismoelectric and electrokinetic wavefields, and to diffusive fields, the method has promoted the collaboration of researchers from different backgrounds, allowing the rapid development of innovative techniques and applications. It is likely that this cooperation will significantly benefit many of the Earth-related sciences. Hence, the need for this review is clear: to make this, in parts complex field accessible to Earth scientists in general, and to tectonophysicists in particular.

Acknowledgements

We thank the following researchers for supporting us by providing some of the figures in this paper: Brian Baptie for the global earthquake and receiver distribution map (Fig. 4); Simon King for the interferometric velocity analysis plots (Figs. 18(b), (c), 19); Heather Nicolson for the virtual-receiver seismograms (Fig. 21(b)); Roel Snieder for the Merapi volcano seismograms (Fig. 24). We also thank two reviewers for their constructive comments and suggestions, which improved this paper.

References

- Arroucau, P., Rawlinson, N., Sambridge, M., 2010. New insight into Cainozoic sedimentary basins and Palaeozoic suture zones in southeast Australia from ambient noise surface wave tomography. *Geophysical Research Letters* 37 (7), L07303.
- Bakulin, A., Calvert, R., 2004. Virtual source: new method for imaging and 4D below complex overburden. *SEG Technical Program Expanded Abstracts* 23 (1), 2477–2480.
- Bakulin, A., Calvert, R., 2006. The virtual source method: Theory and case study. *Geophysics* 71 (4), S1139–S1150.
- Bakulin, A., Mateeva, A., Mehta, K., Jorgensen, P., Ferrandis, J., Herhold, I.S., Lopez, J., 2007. Virtual source applications to imaging and reservoir monitoring. *The Leading Edge* 26 (6), 732–740.
- Bensen, G.D., Ritzwoller, M.H., Shapiro, N.M., 2008. Broadband ambient noise surface wave tomography across the United States. *Journal of Geophysical Research* 113 (B5), B05306.
- Born, M., Wolf, E., 1999. *Principles of Optics*. Cambridge University Press, Cambridge.
- Brandon, C., Romanowicz, B., 1986. A "No-Lid" Zone in the Central Chang-Thang Plateau of Tibet: Evidence from Pure Path Phase Velocity Measurements of Long Period Rayleigh Waves. *Journal of Geophysical Research* 91 (B6), 6547–6564.
- Brenguier, F., Shapiro, N.M., Campillo, M., Nercessian, A., Ferrazzini, V., 2007. 3-D surface wave tomography of the Piton de la Fournaise volcano using seismic noise correlations. *Geophysical Research Letters* 34 (2), L02305.
- Brenguier, F., Campillo, M., Hadziioannou, C., Shapiro, N.M., Nadeau, R.M., Larose, E., 2008a. Postseismic Relaxation Along the San Andreas Fault at Parkfield from Continuous Seismological Observations. *Science* 321 (5895), 1478–1481.
- Brenguier, F., Shapiro, N.M., Campillo, M., Ferrazzini, V., Duputel, Z., Coutant, O., Nercessian, A., 2008b. Towards forecasting volcanic eruptions using seismic noise. *Nature Geosci* 1 (2), 126–130.
- Campillo, M., Paul, A., 2003. Long-Range Correlations in the Diffuse Seismic Coda. *Science* 299 (5606), 547–549.
- Cho, K.H., Herrmann, R.B., Ammon, C.J., Lee, K., 2007. Imaging the Upper Crust of the Korean Peninsula by Surface-Wave Tomography. *Bulletin of the Seismological Society of America* 97 (1B), 198–207.
- Claerbout, J.F., 1968. Synthesis of a layered medium from its acoustic transmission response. *Geophysics* 33 (2), 264–269.
- Claerbout, J.F., 1976. *Fundamentals of Geophysical Data Processing*. Blackwell Scientific Publications.
- Cole, S., 1995. *Passive seismic and drill-bit experiments using 2-D arrays*. PhD Thesis, Stanford University.
- Curtis, A., 2009. Source-receiver seismic interferometry. *SEG Technical Program Expanded Abstracts* 28 (1), 3655–3659.
- Curtis, A., Halliday, D., 2010a. Source-receiver wave field interferometry. *Physical Review E* 81 (4), 046601.
- Curtis, A., Halliday, D., 2010b. Directional balancing for seismic and general wavefield interferometry. *Geophysics* 75 (1), SA1–SA14.
- Curtis, A., Woodhouse, J.H., 1997. Crust and upper mantle shear velocity structure beneath the Tibetan plateau and surrounding regions from interevent surface wave phase velocity inversion. *Journal of Geophysical Research* 102 (B6), 11789–11813.
- Curtis, A., Gerstoft, P., Sato, H., Snieder, R., Wapenaar, K., 2006. Seismic interferometry—turning noise into signal. *The Leading Edge* 25 (9), 1082–1092.
- Curtis, A., Nicolson, H., Halliday, D., Trampert, J., Baptie, B., 2009. Virtual seismometers in the subsurface of the Earth from seismic interferometry. *Nature Geosci* 2 (10), 700–704.
- de Hoop, A.T., 1988. Time-domain reciprocity theorems for acoustic wave fields in fluids with relaxation. *The Journal of the Acoustical Society of America* 84 (5), 1877–1882.
- Derode, A., Larose, E., Campillo, M., Fink, M., 2003a. How to estimate the Green's function of a heterogeneous medium between two passive sensors? Application to acoustic waves. *Applied Physics Letters* 83 (15), 3054–3056.
- Derode, A., Larose, E., Tanter, M., de Rosny, J., Tourin, A., Campillo, M., Fink, M., 2003b. Recovering the Green's function from field-field correlations in an open scattering medium (L). *The Journal of the Acoustical Society of America* 113 (6), 2973–2976.
- Dong, S., He, R., Schuster, G.T., 2006. Interferometric prediction and least squares subtraction of surface waves. *SEG Technical Program Expanded Abstracts* 25 (1), 2783–2786.
- Douma, H., Snieder, R., 2006. Correcting for bias due to noise in coda wave interferometry. *Geophysical Journal International* 164 (1), 99–108.
- Draganov, D., Wapenaar, K., Thorbecke, J., 2006. Seismic interferometry: Reconstructing the earth's reflection response. *Geophysics* 71 (4), S161–S170.
- Draganov, D., Wapenaar, K., Mulder, W., Singer, J., Verdel, A., 2007. Retrieval of reflections from seismic background-noise measurements. *Geophysical Research Letters* 34 (4), L04305.
- Draganov, D., Campman, X., Thorbecke, J., Verdel, A., Wapenaar, K., 2009. Reflection images from ambient seismic noise. *Geophysics* 74 (5), A63–A67.
- Duguid, C., Halliday, D.F., Curtis, A., 2011. Source-Receiver Interferometry for Seismic Wavefield Construction and Ground Roll Removal. *The Leading Edge* 30 (8), 838–843.
- Duvall, T.L., Jefferies, S.M., Harvey, J.W., Pomerantz, M.A., 1993. Time-distance helioseismology. *Nature* 362 (6419), 430–432.
- Fokkema, J.T., van den Berg, P.M., 1993. *Seismic applications of acoustic reciprocity*. Elsevier Science Publishing Company, Inc. 350 pp.
- Forghani, F., Snieder, R., 2010. Underestimation of body waves and feasibility of surface-wave reconstruction by seismic interferometry. *The Leading Edge* 29 (7), 790–794.

- Gerstoft, P., Sabra, K.G., Roux, P., Kuperman, W.A., Fehler, M.C., 2006. Green's functions extraction and surface-wave tomography from microseisms in southern California. *Geophysics* 71 (4), S123–S131.
- Grechka, V., Dewangan, P., 2003. Generation and processing of pseudo-shear-wave data: Theory and case study. *Geophysics* 68 (6), 1807–1816.
- Grechka, V., Tsvankin, I., 2002. PP + PS = SS. *Geophysics* 67 (6), 1961–1971.
- Grêt, A., Snieder, R., Aster, R.C., Kyle, P.R., 2005. Monitoring rapid temporal change in a volcano with coda wave interferometry. *Geophysical Research Letters* 32 (6), L06304.
- Grêt, A., Snieder, R., Özbay, U., 2006a. Monitoring in situ stress changes in a mining environment with coda wave interferometry. *Geophysical Journal International* 167 (2), 504–508.
- Grêt, A., Snieder, R., Scales, J., 2006b. Time-lapse monitoring of rock properties with coda wave interferometry. *Journal of Geophysical Research* 111 (B3), B03305.
- Gudmundsson, Ö., Khan, A., Voss, P., 2007. Rayleigh-wave group-velocity of the Icelandic crust from correlation of ambient seismic noise. *Geophysical Research Letters* 34 (14), L14314.
- Gurrola, H., Minster, J.B., Owens, T., 1994. The Use of Velocity Spectrum For Stacking Receiver Functions and Imaging Upper Mantle Discontinuities. *Geophysical Journal International* 117 (2), 427–440.
- Halliday, D., 2010. Adaptive model-driven interferometry for ground-roll attenuation. SEG Technical Program Expanded Abstracts 29 (1), 3550–3554.
- Halliday, D., Curtis, A., 2008. Seismic interferometry, surface waves and source distribution. *Geophysical Journal International* 175 (3), 1067–1087.
- Halliday, D., Curtis, A., 2009a. Generalized optical theorem for surface waves and layered media. *Physical Review E* 79 (5), 056603.
- Halliday, D., Curtis, A., 2009b. Seismic interferometry of scattered surface waves in attenuative media. *Geophysical Journal International* 178 (1), 419–446.
- Halliday, D., Curtis, A., 2010. An interferometric theory of source-receiver scattering and imaging. *Geophysics* 75 (6), SA95–SA103.
- Halliday, D.F., Curtis, A., Robertsson, J.O.A., van Manen, D.-J., 2007. Interferometric surface-wave isolation and removal. *Geophysics* 72 (5), A69–A73.
- Halliday, D., Curtis, A., Kragh, E., 2008. Seismic surface waves in a suburban environment: Active and passive interferometric methods. *The Leading Edge* 27 (2), 210–218.
- Halliday, D.F., Curtis, A., Vermeer, P., Strobbia, C., Glushchenko, A., van Manen, D.J., Robertsson, J.O.A., 2010a. Interferometric ground-roll removal: Attenuation of scattered surface waves in single-sensor data. *Geophysics* 75 (2), SA15–SA25.
- Halliday, D.F., Curtis, A., Wapenaar, K., 2010b. Generalized PP + PS = SS from seismic interferometry. Society of Exploration Geophysics, Annual Meeting.
- Harmon, N., Rychert, C., Gerstoft, P., 2010. Distribution of noise sources for seismic interferometry. *Geophysical Journal International* 183 (3), 1470–1484.
- Heit, B., Yuan, X., Bianchi, M., Sodoudi, F., Kind, R., 2008. Crustal thickness estimation beneath the southern central Andes at 30°S and 36°S from S wave receiver function analysis. *Geophysical Journal International* 174 (1), 249–254.
- Hong, T.-K., Menke, W., 2006. Tomographic investigation of the wear along the San Jacinto fault, southern California. *Physics of The Earth and Planetary Interiors* 155 (3–4), 236–248.
- Kind, R., Vinnik, L.P., 1988. The upper mantle discontinuities underneath the GRF array from P-to-S converted phases. *Journal of Geophysics* 62 (3), 138–147.
- King, S., Curtis, A., 2012. Suppressing nonphysical reflections in Green's function estimates using source-receiver interferometry. *Geophysics* 77 (1), Q15–Q25.
- King, S., Curtis, A., Poole, T.L., 2011. Interferometric velocity analysis using physical and nonphysical energy. *Geophysics* 76 (1), SA35–SA49.
- Kraeva, N., Pinsky, V., Hofstetter, A., 2009. Seasonal variations of cross correlations of seismic noise in Israel. *Journal of Seismology* 13 (1), 73–87.
- Kumar, P., Kind, R., Yuan, X., 2010. Receiver function summation without deconvolution. *Geophysical Journal International* 180 (3), 1223–1230.
- Lagendijk, A., van Tiggelen, B.A., 1996. Resonant multiple scattering of light. *Physics Reports* 270 (3), 143–215.
- Langston, C.A., 1979. Structure Under Mount Rainier, Washington, Inferred From Teleseismic Body Waves. *Journal of Geophysical Research* 84 (B9), 4749–4762.
- Larose, E., Derode, A., Clouvenec, D., Margerin, L., Campillo, M., 2005. Passive retrieval of Rayleigh waves in disordered elastic media. *Physical Review E* 72 (4), 046607.
- Li, H., Su, W., Wang, C.-Y., Huang, Z., 2009. Ambient noise Rayleigh wave tomography in western Sichuan and eastern Tibet. *Earth and Planetary Science Letters* 282 (1–4), 201–211.
- Li, H., Bernardi, F., Michelini, A., 2010a. Love wave tomography in Italy from seismic ambient noise. *Earthquake Science* 23 (5), 487–495.
- Li, H., Su, W., Wang, C.-Y., Huang, Z., Lv, Z., 2010b. Ambient noise Love wave tomography in the eastern margin of the Tibetan plateau. *Tectonophysics* 491 (1–4), 194–204.
- Liang, C., Langston, C.A., 2008. Ambient seismic noise tomography and structure of eastern North America. *Journal of Geophysical Research* 113 (B3), B03309.
- Lin, F.-C., Ritzwoller, M.H., Townend, J., Bannister, S., Savage, M.K., 2007. Ambient noise Rayleigh wave tomography of New Zealand. *Geophysical Journal International* 170 (2), 649–666.
- Lin, F.-C., Moschetti, M.P., Ritzwoller, M.H., 2008. Surface wave tomography of the western United States from ambient seismic noise: Rayleigh and Love wave phase velocity maps. *Geophysical Journal International* 173 (1), 281–298.
- Lobkis, O.I., Weaver, R.L., 2001. On the emergence of the Green's function in the correlations of a diffuse field. *The Journal of the Acoustical Society of America* 110 (6), 3011–3017.
- Lu, R., Willis, M., Campman, X., Ajo-Franklin, J., Toksoz, M.N., 2008. Redatuming through a salt canopy and target-oriented salt-flank imaging. *Geophysics* 73 (3), S63–S71.
- Maret, G., 1995. In: Akkermans, E., Montambaux, G., Pichard, J.L., Zinn-Justin, J. (Eds.), *Mesoscopic Quantum Physics*. Amsterdam, Elsevier Science.
- Mehta, K., Bakulin, A., Sheiman, J., Calvert, R., Snieder, R., 2007. Improving the virtual source method by wavefield separation. *Geophysics* 72 (4), V79–V86.
- Mehta, K., Sheiman, J.L., Snieder, R., Calvert, R., 2008. Strengthening the virtual-source method for time-lapse monitoring. *Geophysics* 73 (3), S73–S80.
- Mikesell, D., van Wijk, K., Calvert, A., Haney, M., 2009. The virtual refraction: Useful spurious energy in seismic interferometry. *Geophysics* 74 (3), A13–A17.
- Minato, S., Matsuoka, T., Tsuji, T., Draganov, D., Hunziker, J., Wapenaar, K., 2011. Seismic interferometry using multidimensional deconvolution and crosscorrelation for crosswell seismic reflection data without borehole sources. *Geophysics* 76 (1), SA19–SA34.
- Miyazawa, M., Snieder, R., Venkataraman, A., 2008. Application of seismic interferometry to extract P- and S-wave propagation and observation of shear-wave splitting from noise data at Cold Lake, Alberta, Canada. *Geophysics* 73 (4), D35–D40.
- Moschetti, M.P., Ritzwoller, M.H., Shapiro, N.M., 2007. Surface wave tomography of the western United States from ambient seismic noise: Rayleigh wave group velocity maps. *Geochemistry, Geophysics, Geosystems* 8 (8), Q08010.
- Nagaoka, Y., Nishida, K., Aoki, Y., Takeo, M., 2010. Temporal change of phase velocity beneath Mt. Asama, Japan, inferred from coda wave interferometry. *Geophysical Research Letters* 37 (22), L22311–L.
- Neidell, N.S., Taner, M.T., 1971. Semblance and other coherency measures for multi-channel data. *Geophysics* 36 (3), 482–497.
- Nicolson, H., Curtis, A., Baptie, B., Galetti, E., 2012. Seismic interferometry and ambient noise tomography in the British Isles. *Proceedings of the Geologists' Association* 123 (1), 74–86.
- Ohmi, S., Hirahara, K., Wada, H., Ito, K., 2008. Temporal variations of crustal structure in the source region of the 2007 Noto Hanto Earthquake, central Japan, with passive image interferometry. *Earth Planets Space* 60, 1069–1074.
- Oristaglio, M.L., 1989. An inverse scattering formula that uses all the data. *Inverse Problems* 5, 1097–1105.
- Pandolfi, D., Bean, C.J., Saccorotti, G., 2006. Coda wave interferometric detection of seismic velocity changes associated with the 1999 M = 3.6 event at Mt. Vesuvius. *Geophys. Res. Lett.*, 33. 6, p. L06306.
- Phinney, R.A., 1964. Structure of the Earth's Crust from Spectral Behavior of Long-Period Body Waves. *Journal of Geophysical Research* 69 (14), 2997–3017.
- Poliannikov, O.V., 2011. Retrieving reflections by source-receiver wavefield interferometry. *Geophysics* 76 (1), SA1–SA8.
- Rawlinson, N., Sambridge, M., Saygin, E., 2008. A dynamic objective function technique for generating multiple solution models in seismic tomography. *Geophysical Journal International* 174 (1), 295–308.
- Rayleigh, J.W.S., 1878. *The Theory of Sound*, 2. Dover Publications Inc, New York. 504 pp.
- Rickett, J., Claerbout, J., 1999. Acoustic daylight imaging via spectral factorization; helioseismology and reservoir monitoring. *The Leading Edge* 18 (8), 957–960.
- Romanowicz, B.A., 1982. Constraints on the structure of the Tibet Plateau from pure path phase velocities of Love and Rayleigh waves. *Journal of Geophysical Research* 87 (B8), 6865–6883.
- Ruigrok, E., Campman, X., Draganov, D., Wapenaar, K., 2010. High-resolution lithospheric imaging with seismic interferometry. *Geophysical Journal International* 183 (1), 339–357.
- Ryberg, T., Weber, M., 2000. Receiver function arrays: a reflection seismic approach. *Geophysical Journal International* 141 (1), 1–11.
- Sabra, K.G., Gerstoft, P., Roux, P., Kuperman, W.A., Fehler, M.C., 2005. Surface wave tomography from microseisms in Southern California. *Geophysical Research Letters* 32 (14), L14311.
- Sava, P., Vasconcelos, I., 2009. Efficient computation of extended images by wavefield-based migration. SEG Technical Program Expanded Abstracts 28 (1), 2824–2828.
- Saygin, E., Kennett, B.L.N., 2010. Ambient seismic noise tomography of Australian continent. *Tectonophysics* 481 (1–4), 116–125.
- Schuster, G.T., 2001. *Theory of Daylight/Interferometric Imaging - Tutorial*. EAGE, Extended Abstracts, 63rd EAGE Conference & Exhibition, p. A32.
- Schuster, G.T., Yu, J., Sheng, J., Rickett, J., 2004. Interferometric/daylight seismic imaging. *Geophysical Journal International* 157 (2), 838–852.
- Sens-Schönfelder, C., Wegler, U., 2006. Passive image interferometry and seasonal variations of seismic velocities at Merapi Volcano, Indonesia. *Geophysical Research Letters* 33 (21), L21302.
- Shapiro, N.M., Campillo, M., 2004. Emergence of broadband Rayleigh waves from correlations of the ambient seismic noise. *Geophysical Research Letters* 31 (7), L07614.
- Shapiro, N.M., Campillo, M., Stehly, L., Ritzwoller, M.H., 2005. High-Resolution Surface-Wave Tomography from Ambient Seismic Noise. *Science* 307 (5715), 1615–1618.
- Slob, E., Wapenaar, K., 2007. Electromagnetic Green's functions retrieval by cross-correlation and cross-convolution in media with losses. *Geophysical Research Letters* 34 (5), L05307.
- Slob, E., Draganov, D., Wapenaar, K., 2007. Interferometric electromagnetic Green's functions representations using propagation invariants. *Geophysical Journal International* 169 (1), 60–80.
- Snieder, R., 2003. Coda wave interferometry. In: McGraw-Hill (Ed.), *McGraw-Hill 2004 Yearbook of Science & Technology*. McGraw-Hill, New York.
- Snieder, R., 2004. Extracting the Green's function from the correlation of coda waves: A derivation based on stationary phase. *Physical Review E* 69 (4), 046610.
- Snieder, R., 2006. *The Theory of Coda Wave Interferometry*. Pure and Applied Geophysics 163 (2), 455–473.
- Snieder, R., Hagerty, M., 2004. Monitoring change in volcanic interiors using coda wave interferometry: Application to Arenal Volcano, Costa Rica. *Geophysical Research Letters* 31 (9), L09608.

- Sniieder, R., Grêt, A., Douma, H., Scales, J., 2002. Coda Wave Interferometry for Estimating Nonlinear Behavior in Seismic Velocity. *Science* 295 (5563), 2253–2255.
- Sniieder, R., Wapenaar, K., Larner, K., 2006. Spurious multiples in seismic interferometry of primaries. *Geophysics* 71 (4), S1111–S1124.
- Sniieder, R., Wapenaar, K., Wegler, U., 2007. Unified Green's function retrieval by cross-correlation: connection with energy principles. *Physical Review E* 75 (3), 036103.
- Sniieder, R., van Wijk, K., Haney, M., Calvert, R., 2008. Cancellation of spurious arrivals in Green's function extraction and the generalized optical theorem. *Physical Review E* 78 (3), 036606.
- Sniieder, R., Miyazawa, M., Slob, E., Vasconcelos, I., Wapenaar, K., 2009. A Comparison of Strategies for Seismic Interferometry. *Surveys in Geophysics* 30 (4), 503–523.
- Stehly, L., Campillo, M., Froment, B., Weaver, R.L., 2008. Reconstructing Green's function by correlation of the coda of the correlation (C3) of ambient seismic noise. *Journal of Geophysical Research* 113 (B11), B11306.
- Stehly, L., Fry, B., Campillo, M., Shapiro, N.M., Guilbert, J., Boschi, L., Giardini, D., 2009. Tomography of the Alpine region from observations of seismic ambient noise. *Geophysical Journal International* 178 (1), 338–350.
- Taira, T., Silver, P.G., Niu, F., Nadeau, R.M., 2009. Remote triggering of fault-strength changes on the San Andreas fault at Parkfield. *Nature* 461 (7264), 636–639.
- Thorbecke, J., Wapenaar, K., 2007. On the relation between seismic interferometry and the migration resolution function. *Geophysics* 72 (6), T61–T66.
- Tonegawa, T., Nishida, K., 2010. Inter-source body wave propagations derived from seismic interferometry. *Geophysical Journal International* 183 (2), 861–868.
- Tonegawa, T., Nishida, K., Watanabe, T., Shiomi, K., 2009. Seismic interferometry of teleseismic S-wave coda for retrieval of body waves: an application to the Philippine Sea slab underneath the Japanese Islands. *Geophysical Journal International* 178 (3), 1574–1586.
- van der Neut, J., Bakulin, A., 2008. The effects of time-gating and radiation correction on virtual source data. *SEG Technical Program Expanded Abstracts* 27 (1), 2922–2926.
- van Manen, D.-J., 2006. Time reversal and Interferometry with applications to forward modeling of wave propagation and a chapter on receiver functions. Ph.D. Thesis, University of Edinburgh.
- van Manen, D.-J., Robertsson, J.O.A., Curtis, A., Ferber, R., Paulssen, H., 2003. Shear wave statics using receiver functions. *Geophysical Journal International* 153 (3), F1–F5.
- van Manen, D.-J., Robertsson, J.O.A., Curtis, A., 2005. Modeling of Wave Propagation in Inhomogeneous Media. *Physical Review Letters* 94 (16), 164301.
- van Manen, D.-J., Curtis, A., Robertsson, J.O.A., 2006. Interferometric modeling of wave propagation in inhomogeneous elastic media using time reversal and reciprocity. *Geophysics* 71 (4), S147–S160.
- van Manen, D.-J., Robertsson, J.O.A., Curtis, A., 2007. Exact wave field simulation for finite-volume scattering problems. *The Journal of the Acoustical Society of America* 122 (4), EL115–EL121.
- Vasconcelos, I., 2008. Generalized representations of perturbed fields – applications in seismic interferometry and migration. *SEG Technical Program Expanded Abstracts* 27 (1), 2927–2931.
- Vasconcelos, I., Sniieder, R., 2008a. Interferometry by deconvolution: Part 1 – Theory for acoustic waves and numerical examples. *Geophysics* 73 (3), S115–S128.
- Vasconcelos, I., Sniieder, R., 2008b. Interferometry by deconvolution: Part 2 – Theory for elastic waves and application to drill-bit seismic imaging. *Geophysics* 73 (3), S129–S141.
- Vasconcelos, I., Sava, P., Douma, H., 2009a. Wave-equation extended images via image-domain interferometry. *SEG Technical Program Expanded Abstracts* 28 (1), 2839–2843.
- Vasconcelos, I., Sniieder, R., Douma, H., 2009b. Representation theorems and Green's function retrieval for scattering in acoustic media. *Physical Review E* 80 (3), 036605.
- Vasconcelos, I., Sava, P., Douma, H., 2010. Nonlinear extended images via image-domain interferometry. *Geophysics* 75 (6), SA105–SA115.
- Villaseñor, A., Yang, Y., Ritzwoller, M.H., Gallart, J., 2007. Ambient noise surface wave tomography of the Iberian Peninsula: Implications for shallow seismic structure. *Geophysical Research Letters* 34 (11), L11304.
- Vinnik, L.P., 1977. Detection of waves converted from P to SV in the mantle. *Physics of The Earth and Planetary Interiors* 15 (1), 39–45.
- Wapenaar, K., 2003. Synthesis of an inhomogeneous medium from its acoustic transmission response. *Geophysics* 68 (5), 1756–1759.
- Wapenaar, K., 2004. Retrieving the Elastodynamic Green's Function of an Arbitrary Inhomogeneous Medium by Cross Correlation. *Physical Review Letters* 93 (25), 254301.
- Wapenaar, K., 2007. General representations for wavefield modeling and inversion in geophysics. *Geophysics* 72 (5), SM5–SM17.
- Wapenaar, K., Fokkema, J., 2006. Green's function representations for seismic interferometry. *Geophysics* (4), SI33–SI46.
- Wapenaar, K., van der Neut, J., 2010. A representation for Green's function retrieval by multidimensional deconvolution. *The Journal of the Acoustical Society of America* 128 (6), EL366–EL371.
- Wapenaar, K., Fokkema, J., Sniieder, R., 2005. Retrieving the Green's function in an open system by cross correlation: A comparison of approaches (L). *The Journal of the Acoustical Society of America* 118 (5), 2783–2786.
- Wapenaar, K., Slob, E., Sniieder, R., 2006. Unified Green's Function Retrieval by Cross Correlation. *Physical Review Letters* 97 (23), 234301.
- Wapenaar, K., van der Neut, J., Ruigrok, E., 2008. Passive seismic interferometry by multidimensional deconvolution. *Geophysics* 73 (6), A51–A56.
- Wapenaar, K., Draganov, D., Sniieder, R., Campman, X., Verdel, A., 2010a. Tutorial on seismic interferometry: Part 1 – Basic principles and applications. *Geophysics* 75 (5), 75A195–75A209.
- Wapenaar, K., Slob, E., Sniieder, R., 2010b. On seismic interferometry, the generalized optical theorem, and the scattering matrix of a point scatterer. *Geophysics* 75 (3), SA27–SA35.
- Wapenaar, K., Slob, E., Sniieder, R., Curtis, A., 2010c. Tutorial on seismic interferometry: Part 2 – Underlying theory and new advances. *Geophysics* 75 (5), 75A211–75A227.
- Wapenaar, K., Ruigrok, E., van der Neut, J., Draganov, D., 2011. Improved surface-wave retrieval from ambient seismic noise by multi-dimensional deconvolution. *Geophysical Research Letters* 38 (1), L01313.
- Weaver, R.L., Lobkis, O.I., 2001. Ultrasonics without a Source: Thermal Fluctuation Correlations at MHz Frequencies. *Physical Review Letters* 87 (13), 134301.
- Wegler, U., Sens-Schönfelder, C., 2007. Fault zone monitoring with passive image interferometry. *Geophysical Journal International* 168 (3), 1029–1033.
- Wegler, U., Nakahara, H., Sens-Schönfelder, C., Korn, M., Shiomi, K., 2009. Sudden drop of seismic velocity after the 2004 Mw 6.6 mid-Niigata earthquake, Japan, observed with Passive Image Interferometry. *Journal of Geophysical Research* 114 (B6), B06305.
- Yang, Y., Ritzwoller, M.H., Levshin, A.L., Shapiro, N.M., 2007. Ambient noise Rayleigh wave tomography across Europe. *Geophysical Journal International* 168 (1), 259–274.
- Yang, Y., Li, A., Ritzwoller, M.H., 2008. Crustal and uppermost mantle structure in southern Africa revealed from ambient noise and teleseismic tomography. *Geophysical Journal International* 174 (1), 235–248.
- Yao, H., Van Der Hilst, R.D., De Hoop, M.V., 2006. Surface-wave array tomography in SE Tibet from ambient seismic noise and two-station analysis – I. Phase velocity maps. *Geophysical Journal International* 166 (2), 732–744.
- Yao, H., Beghein, C., Van Der Hilst, R.D., 2008. Surface wave array tomography in SE Tibet from ambient seismic noise and two-station analysis – II. Crustal and upper-mantle structure. *Geophysical Journal International* 173 (1), 205–219.
- Zhan, Z., Ni, S., Helmberger, D.V., Clayton, R.W., 2010. Retrieval of Moho-reflected shear wave arrivals from ambient seismic noise. *Geophysical Journal International* 182 (1), 408–420.
- Zheng, S., Sun, X., Song, X., Yang, Y., Ritzwoller, M.H., 2008. Surface wave tomography of China from ambient seismic noise correlation. *Geochemistry, Geophysics, Geosystems* 9 (5), Q05020.
- Zheng, X., Jiao, W., Zhang, C., Wang, L., 2010. Short-Period Rayleigh-Wave Group Velocity Tomography through Ambient Noise Cross-Correlation in Xinjiang, Northwest China. *Bulletin of the Seismological Society of America* 100 (3), 1350–1355.
- Zhou, R., Huang, L., Rutledge, J.T., Fehler, M., Daley, T.M., Majer, E.L., 2010. Coda-wave interferometry analysis of time-lapse VSP data for monitoring geological carbon sequestration. *International Journal of Greenhouse Gas Control* 4 (4), 679–686.